The Astrophysical Journal, 879:120 (20pp), 2019 July 10 https://doi.org/10.3847/1538-4357/ab24cd

HALO7D II: The Halo Velocity Ellipsoid and Velocity Anisotropy with Distant Main-sequence Stars

Emily C. Cunningham[1], Alis J. Deason[2], Robyn E. Sanderson[3,4], Sangmo Tony Sohn[5], Jay Anderson[5], Puragra Guhathakurta[1], Constance M. Rockosi[1], Roeland P. van der Marel[5,6], Sarah R. Loebman[7], and Andrew Wetzel[7]
[1] Department of Astronomy & Astrophysics, University of California, Santa Cruz, 1156 High Street, Santa Cruz, CA 95064, USA
[2] Institute for Computational Cosmology, Department of Physics, University of Durham, South Road, Durham DH1 3LE, UK
[3] Department of Physics & Astronomy, University of Pennsylvania, 209 S 33rd St., Philadelphia, PA 19104, USA
[4] Center for Computational Astrophysics, Flatiron Institute, 162 5th Ave., New York, NY 10010, USA
[5] Space Telescope Science Institute, 3700 San Martin Drive, Baltimore, MD 21218, USA
[6] Center for Astrophysical Sciences, Department of Physics & Astronomy, Johns Hopkins University, Baltimore, MD 21218, USA
[7] Department of Physics, University of California, Davis, CA 95616, USA
Received 2018 October 29; revised 2019 April 30; accepted 2019 May 24; published 2019 July 15

Abstract

The Halo Assembly in Lambda Cold Dark Matter: Observations in 7 Dimensions (HALO7D) data set consists of Keck II/DEIMOS spectroscopy and *Hubble Space Telescope*–measured proper motions of Milky Way halo main-sequence turnoff stars in the CANDELS fields. In this paper, the second in the HALO7D series, we present the proper motions for the HALO7D sample. We discuss our measurement methodology, which makes use of a Bayesian mixture modeling approach for creating the stationary reference frame of distant galaxies. Using the 3D kinematic HALO7D sample, we estimate the parameters of the halo velocity ellipsoid, $\langle v_\phi \rangle$, σ_r, σ_ϕ, σ_θ, and the velocity anisotropy β. Using the full HALO7D sample, we find $\beta = 0.68^{+0.04}_{-0.05}$ at $\langle r \rangle = 23$ kpc. We also estimate the ellipsoid parameters for our sample split into three apparent magnitude bins; the posterior medians for these estimates of β are consistent with one another. Finally, we estimate β in each of the individual HALO7D fields. We find that the velocity anisotropy β can vary from field-to field, which suggests that the halo is not phase-mixed at $\langle r \rangle = 23$ kpc. We explore the β variation across the skies of two stellar halos from the *Latte* suite of FIRE-2 simulations, finding that both simulated galaxies show β variation over a range similar to that of the variation observed across the four HALO7D fields. The accretion histories of the two simulated galaxies result in different β variation patterns; spatially mapping β is thus a way forward in characterizing the accretion history of the Galaxy.

Key words: Galaxy: halo – Galaxy: kinematics and dynamics – methods: statistical – proper motions

1. Introduction

The Milky Way (MW) stellar halo's kinematic structure contains key clues about the Galaxy's formation and mass assembly. According to the Lambda Cold Dark Matter paradigm for the evolution of the universe, the MW has built up its halo of dark matter over cosmic time by accreting smaller dark matter halos, some of which host dwarf galaxies. The remnants of these accreted dwarfs are found in the Milky Way's stellar halo, and the velocities of these stars retain a link to their initial conditions because of their long dynamical times. The HALO7D project aims to investigate the MW's formation by studying the chemical and phase-space structure of the stellar halo's distant, main-sequence (MS) stars.

One kinematic quantity that has long been of interest in MW formation studies is the velocity anisotropy β (Binney & Tremaine 2008), which provides a measure of the relative energy in tangential and radial orbits:

$$\beta = 1 - \frac{\langle v_\phi^2 \rangle + \langle v_\theta^2 \rangle}{2\langle v_r^2 \rangle}. \quad (1)$$

Systems with $\beta = 1$ are on completely radial orbits, while a population of stars on perfectly circular orbits has $\beta = -\infty$.

The velocity anisotropy parameter β plays a key role in the spherical Jeans (1915) equation:

$$M_{\rm Jeans}(<r) = -\frac{r\sigma_r^2}{G}\left(\frac{d\ \ln \rho}{d\ \ln r} + \frac{d\ \ln \sigma_r^2}{d\ \ln r} + 2\beta\right). \quad (2)$$

Jeans modeling has been used to estimate the mass of the Galaxy in many studies (e.g., Dehnen et al. 2006; Watkins et al. 2009, 2019; Gnedin et al. 2010; Deason et al. 2012; Eadie et al. 2017; Sohn et al. 2018 and references therein). However, estimates of the MW's mass have long been plagued by the mass-anisotropy degeneracy, owing to the lack of constraints on the tangential velocity distributions. It has only recently become possible to directly measure the tangential motion of kinematic tracers outside of the solar neighborhood. Previous studies have estimated β from line-of-sight (LOS) velocities alone (e.g., Sirko et al. 2004; Deason et al. 2012; Kafle et al. 2012; King et al. 2015), taking advantage of the fact that, because of our position within the Galaxy, the LOS velocity distribution contains information about the tangential velocity distributions. However, as pointed out by Hattori et al. (2017), studies of stars beyond $r \sim 15$ kpc with only LOS data (where $v_{\rm LOS} \approx v_r$) result in systematic underestimates of β.

Fortunately, measuring tangential properties of tracers is now possible, thanks to the *Hubble Space Telescope* (*HST*) and the *Gaia* mission. The first estimate of β outside the solar neighborhood using directly measured 3D kinematics was presented by Cunningham et al. (2016), hereafter C16, using 13 MS stars with PMs measured from *HST* and radial velocities measured from Keck spectra. We found $\beta = -0.3^{+0.4}_{-0.9}$, consistent with isotropy and lower than solar neighborhood estimates, which find a radially biased $\beta \sim 0.5$–0.7 (Smith et al. 2009; Bond et al. 2010). However, the uncertainties on

this measurement were substantial (primarily due to the small sample size), and in order to better constrain β and the MW mass, more tracers are required.

Studies have recently used the PMs of globular clusters (GCs) as kinematic tracers to estimate β and the mass of the MW. Sohn et al. (2018) used their own *HST* PM measurements of 16 GCs to find $\beta = 0.609^{+0.130}_{-0.229}$ in the Galactocentric distance range of $R_{\rm GC} = 10$–40 kpc, and a corresponding MW virial mass of $M_{\rm MW,virial} = 2.05^{0.97}_{-0.79} \times 10^{12}\,M_{\odot}$. Watkins et al. (2019) used PM determinations of 34 GCs in the range $R_{\rm GC} = 2.0$–21.1 kpc, based on *Gaia* DR2 (Gaia Collaboration et al. 2018b). They found $\beta = 0.48^{+0.15}_{-0.20}$, consistent with Sohn et al. (2018), and a corresponding virial mass of $M_{\rm MW,virial} = 1.41^{1.99}_{-0.52} \times 10^{12}\,M_{\odot}$.

While studies have sought to estimate a single value of β in order to estimate the mass of the MW, studies of β can have additional power in constraining the MW's accretion history. For example, the anisotropy radial profile $\beta(r)$ can contain information about the Galaxy's assembly history. In Deason et al. (2013b) and C16, we argued that our isotropic measurement of β, which is lower than both solar neighborhood measurements and distant halo estimates (Deason et al. 2012), indicates a "dip" in the β profile, and that this dip could indicate the presence of a shell.

Loebman et al. (2018) provided a theoretical perspective on this question by studying the β profiles in three suites of simulations, including accretion-only and cosmological hydrodynamic simulations. They found that both types of simulations predict radially biased $\langle\beta\rangle \sim 0.7$ beyond 10 kpc. Only one of the 17 simulations studied had tangentially biased β over a large range of radii at $z = 0$; this extended β dip was the result of a major merger at $z \sim 1$. While the other 16 simulations had radially biased β at $z = 0$, Loebman et al. (2018) found that temporal dips in the β profile could arise. They also found that recently accreted material can result in short-lived dips in β, while the passage of a massive satellite can induce a longer-lived dip in the β profile from the in situ component of the stellar halo. This latter scenario could explain the observed "dip" along the line of sight toward M31, as recent studies of the Triangulum Andromeda overdensity have suggested that its origin may be the disk rather than an accreted satellite (Price-Whelan et al. 2015; Bergemann et al. 2018), and that the event that disturbed the orbits of these disk stars may be the passage of the Sagittarius dwarf (Laporte et al. 2018).

The anisotropy variation across different subpopulations in the halo can also be used to disentangle accretion events. Using 7D measurements from the *Gaia* DR1 and SDSS of local MS stars, Belokurov et al. (2018) found that the relatively metal-rich stars ([Fe/H] > -1.7) show strongly radially biased velocity anisotropy (i.e., "sausage" stars, named thus because of the elongated radial velocity distribution relative to the tangential velocity distribution), while the metal-poor stars display an isotropic velocity distribution. They argue that presence of this radially biased, relatively metal-rich population in the inner halo indicates that the MW experienced a relatively massive, early accretion event. Evidence for this scenario has been bolstered with results from *Gaia* DR2 (Deason et al. 2018; Helmi et al. 2018). Lancaster et al. (2019) showed that the kinematics of the BHBs in *Gaia* DR2 can be modeled by a mixture of two populations: one strongly radially biased and one isotropic. Debris from a massive, radialized dwarf that dominates the inner halo, known as the *Gaia*-Sausage, *Gaia*-Enceladus, or Kraken, is speculated to be responsible for this signature.

Table 1
Summary of HALO7D Field Properties

Field	l (deg)	b (deg)	$v_{l,\odot}$ (km s^{-1})	$v_{b,\odot}$ (km s^{-1})	Median PM Error (mas yr^{-1})
COSMOS	236.8	42.1	−126.0	148.2	0.15
GOODS-N	125.9	54.8	−153.8	−154.2	0.12
GOODS-S	223.6	−54.4	−171.5	−140.8	0.20
EGS	96.4	60.4	−38.7	−209.0	0.18

Note. Galactic coordinates, projection of the sun's velocity in galactic coordinates, and the median PM error (in galactic coordinates) for the four HALO7D fields. Quoted median PM errors are the errors in a single component (e.g., $\mu_l \cos(b)$ or μ_b; we find both components of PM have the same median error bars, to within 0.005 mas yr^{-1}, within a given field).

Thanks to the *Gaia* mission, it is now possible to estimate the β of stars in the MW; however, even with *Gaia* DR2, uncertainties remain substantial at large radii, and even in the the final data release, *Gaia* will provide PMs only for stars brighter than $G \sim 20$. As a result, *Gaia* will only provide PMs for MS stars out to $D \sim 15$ kpc in the halo. Beyond $D \sim 15$ kpc, studies of tangential motion of the stellar halo using *Gaia* PMs will be limited to giants and evolved stars (e.g., Bird et al. 2019; Lancaster et al. 2019). While giants make excellent tracers, due to their bright apparent magnitudes, it is impossible to uniformly select giants from all age and metallicity populations in the halo. Giants are also rare; averaging over large areas of the sky (and thus potential inhomogeneities in the halo) is often required when estimating halo properties with giants.

The HALO7D project seeks to complement the *Gaia* mission by measuring 3D kinematics of distant MW halo MS stars. HALO7D includes both Keck spectroscopy and *HST* PMs for MW halo star candidates in the magnitude range $19 < m_{\rm F606W} < 24.5$. This data set provides a deep, densely sampled view of the garden-variety stars of the MW halo. In the first HALO7D paper (Cunningham et al. 2019; hereafter Paper I), we presented the spectroscopic component of the HALO7D data set. In this paper, the second in the HALO7D series, we introduce the component of proper motion of HALO7D and use our full 3D kinematic sample to study the halo velocity ellipsoid and anisotropy.

In this work, we seek to use the HALO7D data set to estimate the parameters of the velocity ellipsoid, as well as the velocity anisotropy, of distant halo MS stars. This paper is organized as follows. In Section 2, we describe the HALO7D data set and present the HALO7D PM samples. In Section 3, we describe our methodology for estimating the halo velocity ellipsoid parameters from our observables. In Section 4, we present our resulting posterior distributions for ellipsoid parameters and velocity anisotropy. In Section 5, we compare our results to previous work and other studies. In Section 6, we investigate the spatial and radial variation of β for two halos from the *Latte* suite of simulations. We conclude in Section 7. Details on our computational method for deriving PM uncertainties are given in Appendix B; a description of how we tested our ellipsoid parameter model with fake data is given in Appendix C.

Table 2
Summary of the *HST* Programs Used for the PM Measurements in this Paper

Field	Program	P.I.	Filter	Dates
COSMOS	GO-9822	Scoville	F814W	2003 Dec–2004 May
	GO-12440	Faber	F814W	2011 Dec–2012 Feb
	GO-12461	Riess	F814W	2012 Feb–2012 Apr
GOODS-N	GO-9583	Giavalisco	F775W	2002 Nov–2003 May
	GO-9727	Perlmutter	F775W	2004 Apr–2004 Aug
	GO-9728	Riess	F775W	2003 Jun–2004 Sep
	GO-10339	Riess	F775W	2004 Oct–2005 Apr
	GO-11600	Weiner	F775W	2009 Sep–2011 Apr
GOODS-S	GO-9425	Giavalisco	F606W, F850LP	2002 Jul–2003 Feb
	GO-9978	Beckwith	F606W, F850LP	2003 Sep–2004 Jan
	GO-10189	Riess	F606W, F850LP	2004 Sep–2005 Aug
	GO-10340	Riess	F606W, F850LP	2004 Jul–2005 Sep
	GO-11563	Illingworth	F606W, F850LP	2009 Aug–2011 Feb
	GO-12060/1/2	Faber	F606W, F850LP	2010 Aug–2012 Feb
EGS	GO-10134	Davis	F814W	2004 Jun–2005 Mar
	GO-12063	Faber	F814W	2011 Apr–2013 May
	GO-12547	Cooper	F814W	2011 Oct–2013 Feb

2. Data Set

HALO7D consists of Keck/DEIMOS spectroscopy and *HST*-measured PMs of MW MSTO stars in the EGS, COSMOS, GOODS-N, and GOODS-S fields. Coordinates of the HALO7D fields are listed in Table 1. We begin this section by summarizing some of the key details on target selection, survey properties, and radial velocity measurements that are discussed in detail in Paper I; the remainder of this section is devoted to a discussion of the proper motion measurements.

2.1. Keck/DEIMOS Spectroscopy

The HALO7D spectroscopic program was described in detail in Paper, I, but we summarize the key details here.

Candidate halo stars were identified from CMDs. To minimize disk contamination, we selected blue, faint ($19 < m_{\rm F606W} < 24.5$) objects with star-like morphologies. Stars were observed with Keck II/DEIMOS, configured with the 600ZD grating centered at 7200 Å, with the first observations taken in 2014 April and the final observations in 2017 April. We targeted each DEIMOS mask for a minimum of 8 hr of total integration time, up to 24 hr.

The radial velocities for these stars were measured using a new Bayesian hierarchical method called VELOCIRAPTOR. In order to build up a sufficient signal-to-noise ratio on our targets, stars were observed many times, sometimes over the course of years. Different observations of the same star will have different raw velocities; this is due to the motion of the Earth around the Sun (the heliocentric correction) as well as offsets in wavelength solution due to slit miscentering (the *A*-band correction). We used a Bayesian hierarchical model in order to combine these different observations into a single estimate of the star's velocity. For further details on this technique, we refer the reader to Paper I.

2.2. HST *Proper Motions*

The measurement methodology in this work builds upon existing *HST* PM measurement techniques, relying on the key concept that distant galaxies can be used to construct an absolute stationary reference frame (e.g., Mahmud & Anderson 2008). Sohn et al. (2012, 2013, 2017) present detailed descriptions of the state-of-the-art PM measurement techniques used to measure the PMs of Local Group systems with *HST* data. These techniques have been used to measure the PMs of M31 (Sohn et al. 2012), dwarf galaxies Leo I (Sohn et al. 2013), Draco and Sculptor (Sohn et al. 2017); MW GCs (Sohn et al. 2018); and several MW streams (Sohn et al. 2016). The PMs of individual MW halo stars measured with *HST* were first published by Deason et al. (2013b); subsequently, the PMs of individual stars belonging to MW streams were published by Sohn et al. (2015, 2016).

However, the previous Sohn PM studies have typically used only a few *HST* pointings in each study; in that work, they were able to carefully select galaxies by eye that are suitable for use in the reference frame. In order to measure PMs over the full area of the CANDELS fields, we required an approach that could identify "good" galaxies (with well-measured positions) and "bad" galaxies (with poorly measured positions) without relying on visual inspection. We therefore built upon existing PM techniques in this work, implementing a Bayesian mixture model that identifies "good" and "bad" galaxies probabilistically and incorporates this uncertainty into the ultimate measurement of the PMs of the stars in the set of images.

2.2.1. Measuring Proper Motions

In order to measure PMs for the HALO7D targets, we first had to identify the *HST* programs and filters to use for PM measurements. The GOODS, COSMOS, and EGS fields have all been observed multiple times with various setups (detectors + filters). Among them, we selected data that provide astrometric quality sufficient for measuring absolute PMs of individual halo stars. Specifically, data used for our PM measurements meet the following conditions: (1) observations must be obtained with either ACS/WFC or WFC3/UVIS; (2) observations must be in one of the broadband filters F606W, F775W, F814W, or F850LP; (3) time baseline of the multiple epochs must be at least 2 yr; (4) combined exposure time in the shallower epoch must be at least one orbit long; and

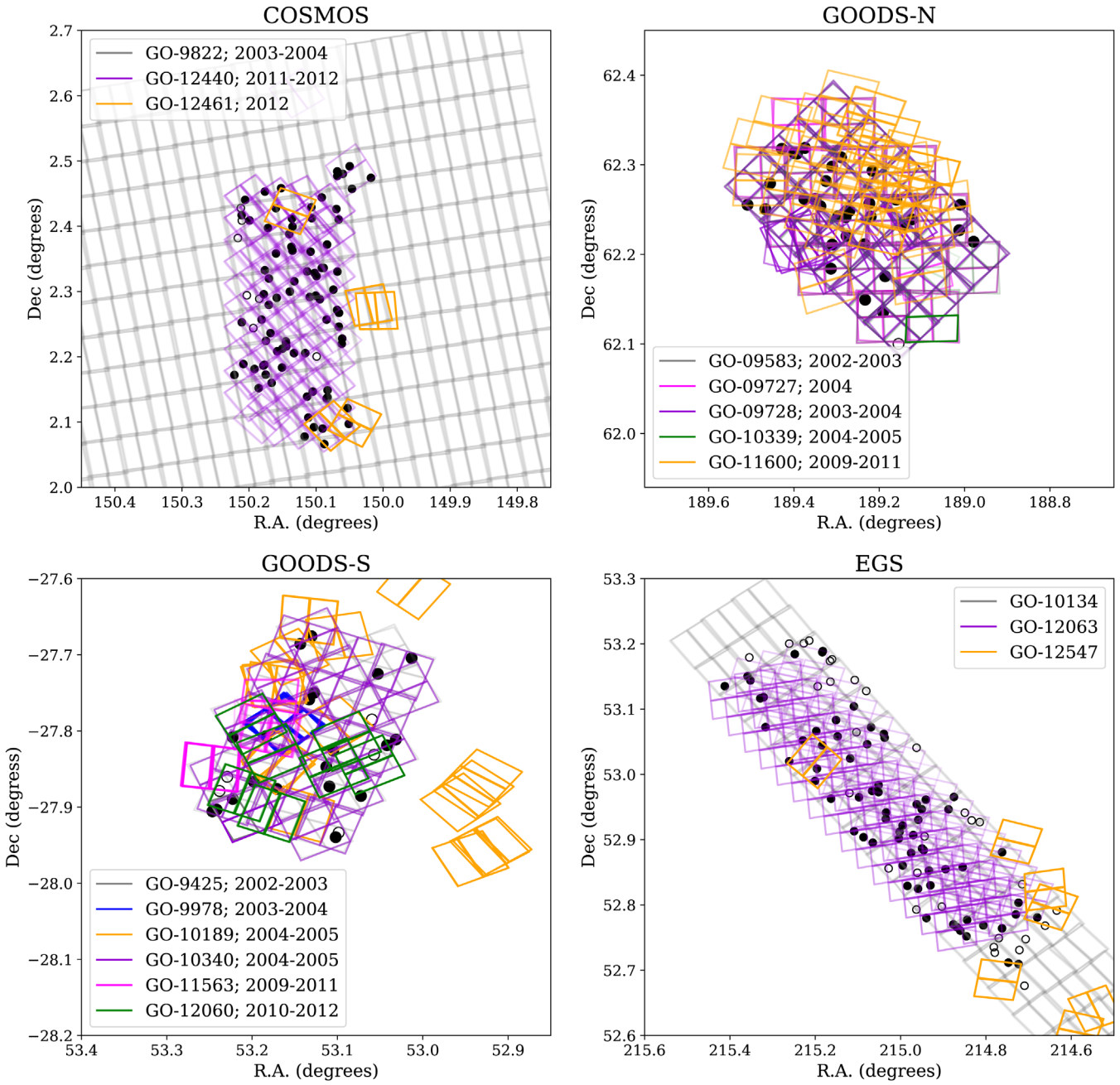

Figure 1. The multi-epoch *HST*/ACS footprints of the four HALO7D fields. Different colors indicate the positions of each ACS chip in the different *HST* programs used to measure PMs in this work. HALO7D spectroscopic targets are indicated by black points; filled points indicate targets for which we successfully measured a PM, whereas empty circles indicate targets for which we could not measure a PM.

(5) individual exposure time must be at least 300 s long. The details of the *HST* programs used for the PM measurements are listed in Table 2; the footprints from these programs are shown in Figure 1.

Once the *HST* programs and filters were chosen, the `*_flc.fits` images were downloaded from MAST. These images are corrected for imperfect charge transfer efficiency using the algorithms described in Anderson & Bedin (2010). The `*_flc.fits` images are processed by a custom-made FORTRAN routine called `flt2xym4rd`, which takes a list of R.A., decl. positions for objects, identifies them in an `flc` image, and measures them with a library PSF (see Anderson & King 2006, AK06), determining for each a position, flux, and stellarity index. The routine then uses the WCS header of each exposure and the distortion solution in AK06 to convert the source positions into an R.A.–decl. frame. This routine is run on all the exposures that cover a particular field.

In this analysis, we measure the PMs on a star-by-star basis. For every target star, the first step is to identify all images that contain the star of interest. The single-exposure catalogs from the `flt2xym4rd` output are then fed into another custom-made routine, `xid2mat`, which takes the single-exposure catalogs in pairs and transforms one catalog into the frame of the other, using the galaxy positions as the basis for the transformation.

Table 3
Velocity Ellipsoid Modeling Results

	$\langle v_\phi \rangle$ (km s^{-1})	σ_ϕ (km s^{-1})	σ_θ (km s^{-1})	σ_r (km s^{-1})	$\langle D \rangle$ (kpc)	$\langle r \rangle$ (kpc)	β	$N_{\rm Stars}$
Full Sample	-13 ± 6	73^{+5}_{-4}	70 ± 4	128 ± 7	20	24	$0.68^{+0.04}_{-0.05}$	199
$19.0 < m_{\rm F606W} < 21.0$	-1^{+13}_{-13}	86^{+10}_{-9}	88^{+14}_{-11}	143^{+13}_{-12}	16	19	$0.61^{+0.08}_{-0.11}$	74
$21.0 < m_{\rm F606W} < 22.5$	-4 ± 9	66^{+7}_{-6}	61^{+7}_{-5}	122^{+11}_{-10}	18	23	$0.72^{+0.05}_{-0.07}$	73
$22.5 < m_{\rm F606W} < 24.5$	-14 ± 9	62^{+8}_{-7}	63^{+8}_{-7}	120^{+13}_{-12}	24	28	$0.71^{+0.07}_{-0.09}$	52
COSMOS	-18 ± 9	74^{+8}_{-7}	61 ± 6	121^{+10}_{-9}	20	25	$0.67^{+0.06}_{-0.08}$	81
GOODS-N	-3^{+17}_{-16}	71^{+13}_{-11}	83^{+23}_{-18}	132^{+20}_{-16}	19	23	$0.64^{+0.12}_{-0.18}$	32
GOODS-S	-40^{+18}_{-17}	65^{+17}_{-12}	125^{+30}_{-22}	116^{+22}_{-17}	18	23	$0.14^{+0.33}_{-0.51}$	20
EGS	-1 ± 10	72^{+8}_{-7}	59^{+7}_{-6}	139^{+13}_{-11}	20	22	$0.77^{+0.05}_{-0.06}$	66

Note. Ellipsoid parameter estimates are quoted for the full sample, for the sample divided into apparent magnitude bins, and the individual HALO7D fields. Posterior medians are quoted, with error bars giving the 16/84 percentiles.

This transformation makes an initial assessment of which galaxies have consistent positions between the two frames, though the ultimate weighting of the galaxies is done in a Bayesian fashion.

We then specify one image as the reference image: the reference image has the maximum amount of overlap with the other images across epochs containing the star of interest. All overlapping images are mapped onto the reference image frame with `xid2mat` using a six-parameter linear transformation:

$$\begin{pmatrix} A & B & x_t \\ C & D & y_t \\ 0 & 0 & 1 \end{pmatrix} \begin{pmatrix} u \\ v \\ 1 \end{pmatrix} = \begin{pmatrix} u_{\rm ref} \\ v_{\rm ref} \\ 1 \end{pmatrix}, \quad (3)$$

where (u, v) are the vectors of distortion-corrected positions of objects in one image and $(u_{\rm ref}, v_{\rm ref})$ are the vectors of positions in the reference image. The parameters x_t, y_t represent any linear translation offset between the two images, while parameters A, B, C, D incorporate scale, rotation, and off-axis linear camera distortion terms. The positions of stars are used to match frames within an epoch, and the positions of "good" galaxies are used to match images across epochs. For more details on why these transformations are required in comparing *HST* images, please see Section 3.6.4 in Anderson & van der Marel (2010).

When the images across epochs have been matched via the linear transformation, the change in the positions of the stars across epochs provides an initial estimate of their PMs. In order to get full posterior probability distributions for the PMs, and incorporate all sources of uncertainty (such as uncertainty in star and galaxy positions, as well as which galaxies should be including in the stationary reference frame), we use a Bayesian mixture modeling approach. We leave as free parameters the positions of all stars and galaxies, the image transformation parameters, and the proper motions of all stars. We model the galaxies in our reference frame as being a mixture of "good" and "bad" galaxies (with poorly measured positions). Within an epoch, we use the positions of stars to precisely align the images.

Table 1 lists the resulting median PM errors in each of the HALO7D fields. Our PM errors are not a function of the magnitudes of our stars, but rather our ability to define the stationary reference frame for a given target. This is determined by how many images there are containing a given star, how much these images overlap across epochs, and how many "good" galaxies there are in the images. For a full description of the Bayesian model for this problem, as well as the details of the Gibbs sampling algorithm we used to sample from the full posterior, we refer the reader to Appendix B.

2.2.2. Proper Motion Diagrams

Figure 1 shows positions of the HALO7D spectroscopic sample as black points; filled circles indicate targets for which we successfully measured PMs, and open circles are stars for which we could not measure a PM. As can be seen in Figure 1, the *HST* pointings from different epochs are not well-aligned; this is because we are using archival data for *HST* programs that were not designed with astrometry in mind. As a result, some of the HALO7D targets only have one epoch of *HST* imaging. This usually arises when the target is on the edge of the field, or if the target falls in the ACS chip gap in one of the epochs.

PM diagrams for the four HALO7D fields are shown in the top panels of Figure 2. PMs are plotted in PMW $= -\mu_\alpha \cos(\delta)$, PMN $= \mu_\delta$. The PMs of HALO7D halo star candidates are shown in pink. Our PM method returns PMs and uncertainties for all point-like objects in the specified reference image that have multi-epoch coverage; PMs for objects that were not HALO7D spectroscopic targets are shown as black points. Most of these points are MW disk stars, though a few will be point-like distant galaxies. As explained in Paper I, our spectroscopically confirmed disk contaminants are white dwarfs (WDs) and red stars with titanium oxide absorption features. These disk contaminants are shown as light blue and orange points, respectively. The black, light blue, and orange points occupy a larger area of PM space than the pink points; because they are mostly disk members, they are at closer distances than the HALO7D halo star candidates and thus have higher proper motions. The PM diagrams as predicted by the Besançon Galaxy Model (Robin et al. 2003), for one square degree fields centered on our field coordinates, are shown in the lower panels of Figure 2 for reference.

In addition, in the EGS field, we had six spectroscopically confirmed quasars for which we could also measure PMs. These PMs are shown in the inset of the upper left-hand panel of Figure 2; reassuringly, all quasar PMs are consistent with 0 mas yr^{-1}.

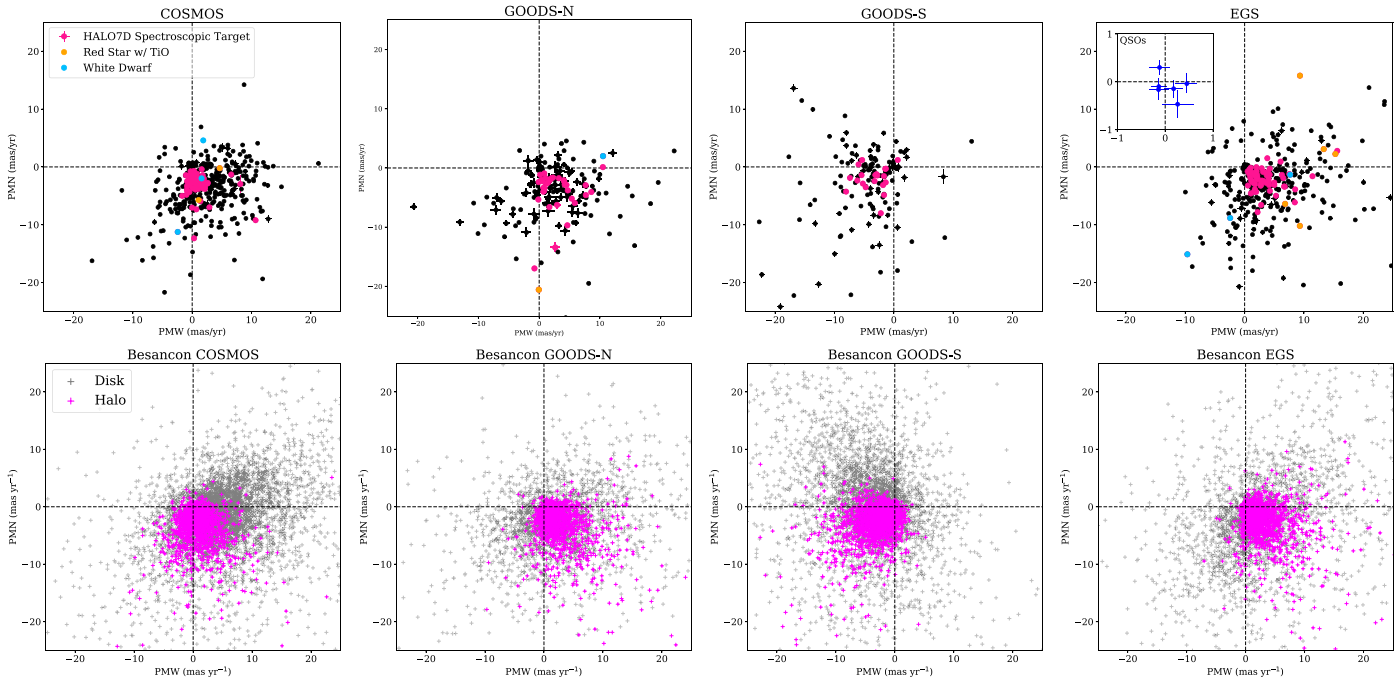

Figure 2. Top panels: proper motion diagrams of the four HALO7D fields. Black points indicate stars that were in the *HST* images that were not HALO7D spectroscopic targets—primarily MW disk stars. HALO7D spectroscopic targets are shown in pink. Light blue points indicate spectroscopically confirmed WDs, while red MW disk star contaminants are shown in orange. In the EGS PM diagram, the inset shows PMs and error bars for six spectroscopically confirmed quasars observed in the EGS field. Lower panels: PM diagrams from the Besançon Galaxy Model, from 1 square degree fields centered on the coordinates of the HALO7D fields. Gray crosses indicate Besançon disk stars, whereas magenta crosses are Besançon halo stars.

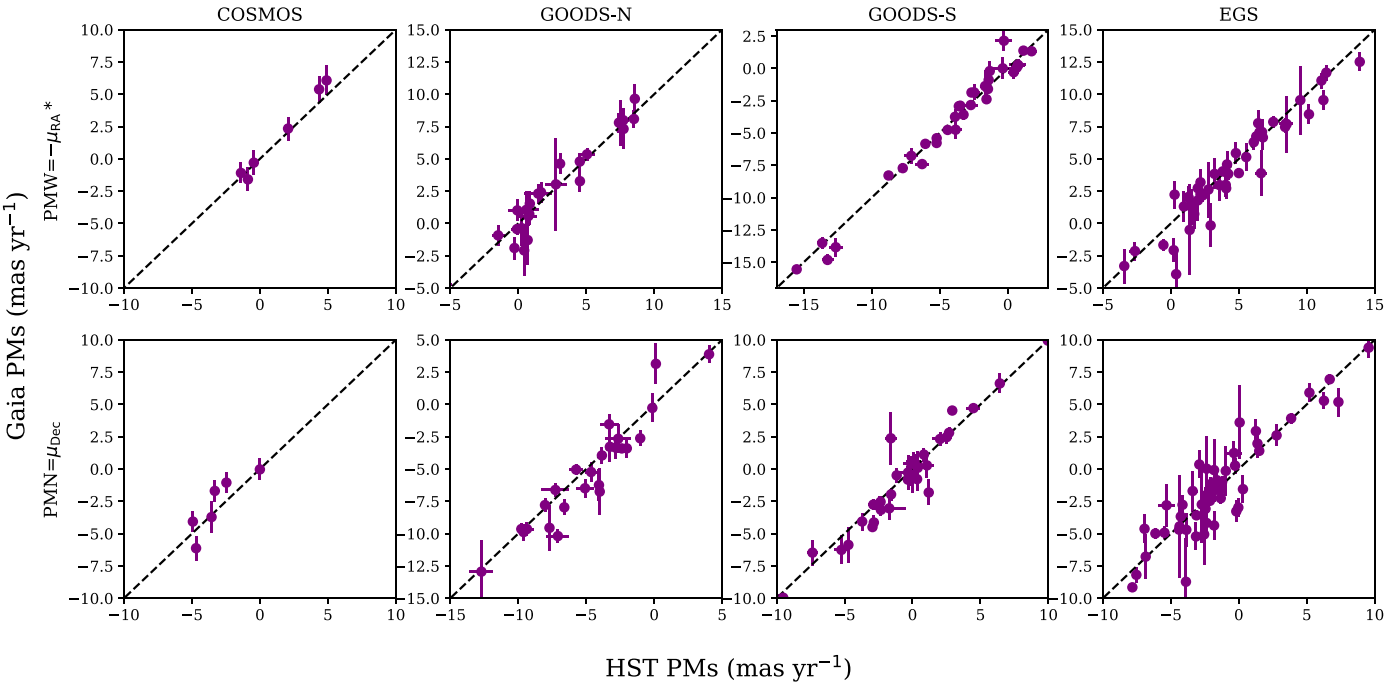

Figure 3. Comparison of the *HST*-measured PMs for sources brighter than $v \sim 21$ with their *Gaia* counterparts, if available. Top panels show the comparison of PMW $= -\mu^*_{\rm R.A.}$; lower panels show the comparison of PMN $= \mu_{\rm decl.}$. The two data sets show excellent agreement, with *HST* PMs generally having lower error bars. For clarity, figures are zoomed in to the regions of highest target density; there are several high |PM| sources that are beyond the range of the figures (2/27 stars in GOODS-N; six high |PMW| and four high |PMN| out of 39 matched sources in GOODS-S; and seven high |PMW| and four high |PMN| out of 56 sources in EGS). In addition, the number of targets that overlap across the two data sets is not necessarily a function of the area of the field, because of *Gaia*'s scanning law; for example, there are only six sources with reported PMs in COSMOS, while EGS, GOODS-S and GOODS-N have 56, 39, and 27 matches, respectively.

As an additional verification of our technique, we compare our measured PMs with those reported in the second data release of the *Gaia* mission (Gaia Collaboration et al. 2016, 2018a). The bright end of our sample corresponds to the faint end of the *Gaia* sample; though most of the halo star candidates used for dynamical modeling in this work do not have reported *Gaia*

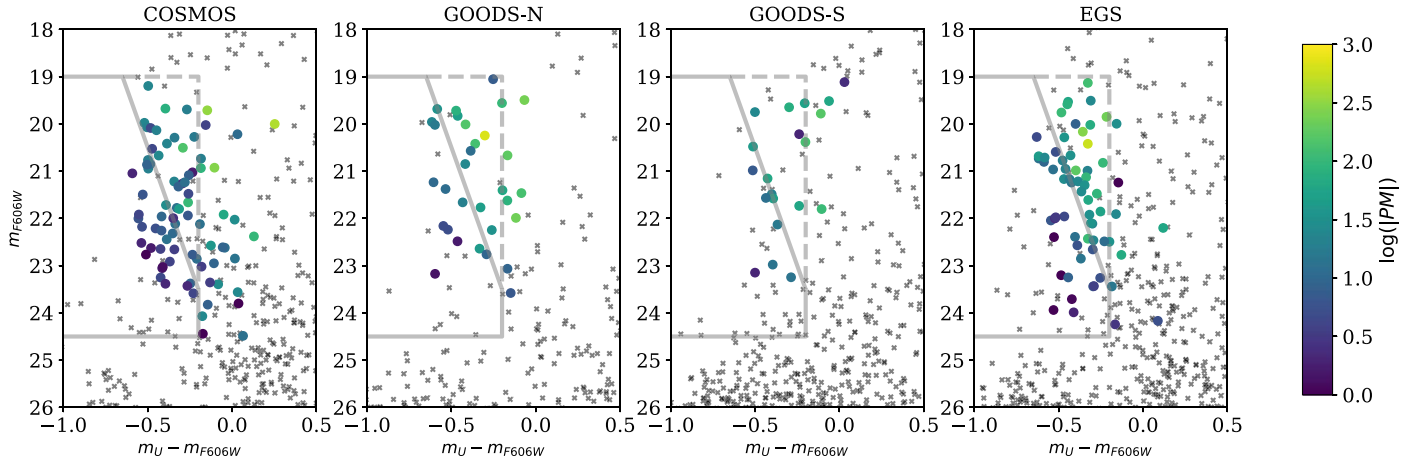

Figure 4. CMDs of the four HALO7D fields, in the STMAG bands F606W and F814W. Gray lines indicate the HALO7D selection boxes for these bandpasses; see Paper I for more details on target selection. Stars used in this analysis (main-sequence stars with successful LOS velocity and PM measurements) are plotted as colored circles, with the colors corresponding to the logarithm of the magnitude of their proper motions ($|\mathrm{PM}|^2 = (\mu_l \cos b)^2 + \mu_b^2$). For the CMDs over the full color range of these fields, please see Figure 3 of Paper I.

PMs, using the full catalog of stars (including stars not targeted for spectroscopy), we find a sizable sample of stars with reported PMs in both data sets.

Figure 3 shows a comparison of the *HST* PMs against the *Gaia* PMs, when available, for sources brighter than $v \sim 21$. Figures are zoomed in to highlight the regions of PM space where there is the highest target density in each field; there are more sources with measured PMs in both catalogs that lie outside the plotted range. We note that the number of sources available for comparison is not necessarily proportional to the area of the field, due to *Gaia* survey incompleteness at the faint end as a result of the *Gaia* scanning law (hence the few overlapping targets in COSMOS). The two data sets show excellent agreement, with the *Gaia* measurements generally having larger error bars. We leave a more detailed comparison of the two data sets (including an exploration of their respective systematics) to future work.

Color magnitude diagrams (CMDs) for the four HALO7D fields are shown in Figure 4. Gray crosses indicate all star candidates, and HALO7D targets with successful PM measurements and LOS velocity measurements are shown as circles color-coded by the magnitude of their PMs ($|\mathrm{PM}|^2 = (\mu_l \cos b)^2 + \mu_b^2$). As expected, bluer, fainter stars tend to have lower PMs (as they are more distant), whereas brighter, redder stars have higher PMs (and are more nearby). For the reader interested in the full color range of the CMD, we refer them to Figure 3 of Paper I.

Our 3D kinematic sample is summarized in Figure 5; PM components in (l, b) are plotted against each other for the four HALO7D fields, color-coded by LOS velocity as measured in Paper I. In EGS, we see an interesting covariance between μ_l and v_{LOS}; there appears to be a trend of increasing LOS velocity with increasing μ_l. However, we note that this is not a signature of rotation. EGS is located at a Galactic longitude $l = 96°$; along this line of sight, $v_l \approx -V_X$, and $V_Y = v_{\mathrm{LOS}} \cos(b) - V_b \sin(b)$. Given that $v_\phi = \frac{x}{R_p} V_Y - \frac{y}{R_p} V_X$, a covariance between V_X, V_Y arises naturally if we assume a Gaussian velocity distribution for v_ϕ. As we will see in Section 4, the fact that v_{LOS} and μ_l increase together is consistent with zero net rotation along this line of sight.

3. Modeling the Halo Velocity Ellipsoid

We use our 3D kinematic sample to estimate the parameters of the halo velocity ellipsoid in spherical coordinates. In this work, we use only objects for which we have both a successful PM measurement and a successful LOS velocity measurement; we leave the analysis of stars with PM measurements but without LOS velocities to future work. Our method is very similar to the ones used in Cunningham et al. (2016) and Deason et al. (2013b), though in this work we have used notation and language consistent with a Bayesian construction of the problem.

For each star i located in field k, we have data $y_i = \{v_{\mathrm{LOS}}, \mu_l, \mu_b\}$, with associated explanatory variables $x_i = \{m_{\mathrm{F606W},i}, m_{\mathrm{F814W},i}, l_k, b_k\}$. We model our sample as being drawn from a mixture of two distributions: the disk distribution (with fixed parameters) and the halo distribution.

The free parameters in our model are the absolute magnitudes (and by extension, the distances) to each star $\boldsymbol{M} = \{M_{\mathrm{F814W},1}, \ldots, M_{\mathrm{F814W},N}\}$ (we denote the corresponding distances $\boldsymbol{D} = \{D_1, \ldots, D_N\}$); the fraction of disk contamination along a given line-of-sight $\boldsymbol{f} = \{f_{\mathrm{Disk},1}, \ldots, f_{\mathrm{Disk},k}\}$; and the halo velocity ellipsoid parameters $\theta_{\mathrm{Halo}} = \{\langle v_\phi \rangle, \sigma_r, \sigma_\phi, \sigma_\theta\}$.

3.1. Disk Model

For the disk model, we work in cylindrical coordinates (R_p, ϕ, z). We assume exponential density profiles in both R_p and z, with a disk scale length of $h_R = 3$ kpc and a disk scale height of $h_z = 1$ kpc.

For the disk velocity distributions, we assume distributions in R_p and z that are Gaussian with zero net motion, and have dispersions of $\sigma_{R_p} = 45\ \mathrm{km\ s^{-1}}$ and $\sigma_z = 20\ \mathrm{km\ s^{-1}}$. For the tangential component, we assume that the rotational velocities are described by a skewed normal distribution with mean $\langle v_T \rangle = 242\ \mathrm{km\ s^{-1}}$, scale parameter $46.2\ \mathrm{km\ s^{-1}}$, and shape parameter of -2. These parameters are derived based on the predicted marginalized velocity distributions from `galpy`[8] (Bovy 2015), using the quasi-isothermal distribution function discussed in Binney (2010) and Binney & McMillan (2011) and the `MWPotential2014` (see Bovy 2015 for details).

[8] http://github.com/jobovy/galpy

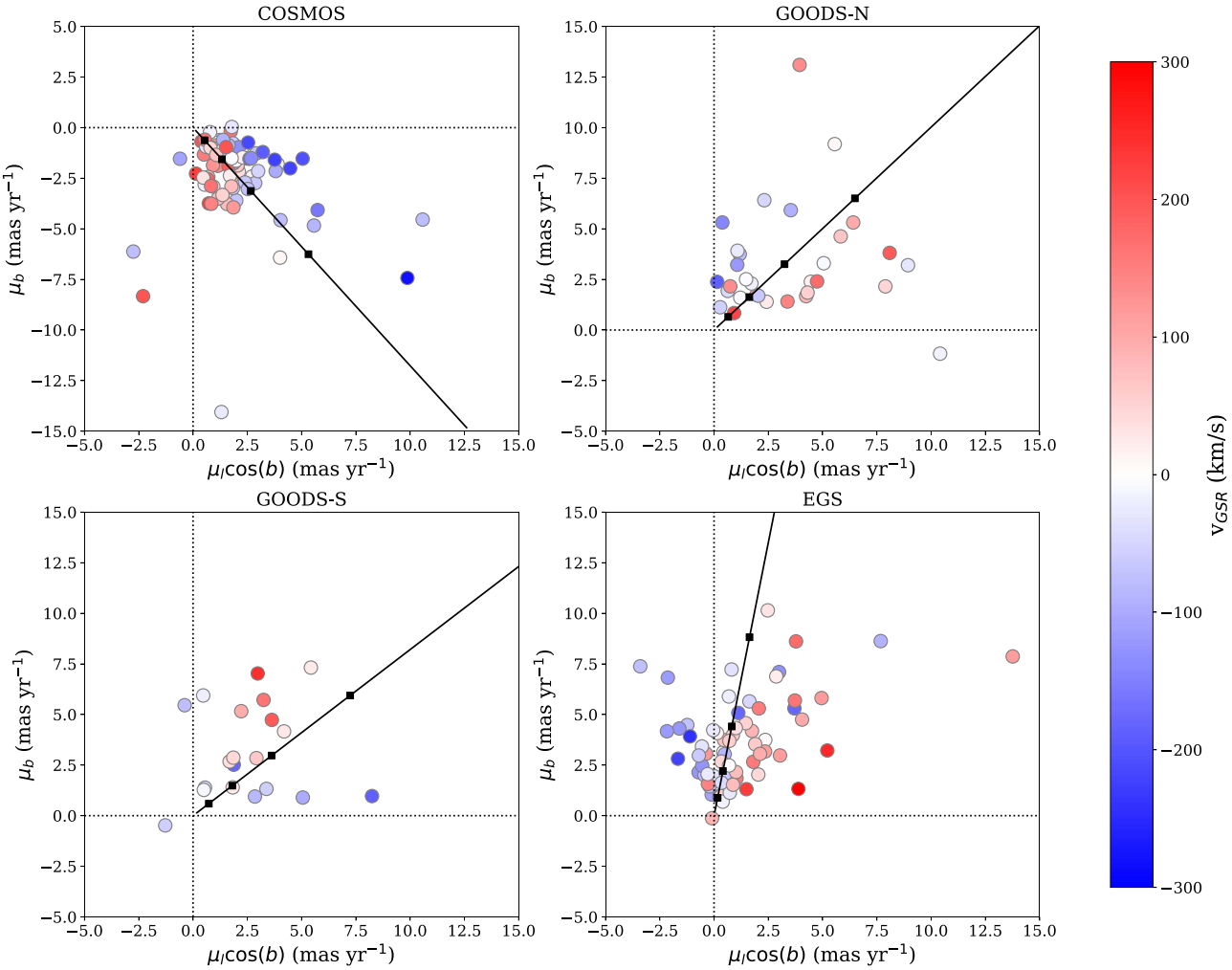

Figure 5. Proper motion diagrams of the four HALO7D fields, in Galactic coordinates, color-coded by LOS velocity in the Galactocentric frame. Solid black lines indicate the solar reflex motion along each sightline; the squares indicate the implied mean PM along each line of sight for $D = 5$, 10, 20, 50 kpc (with mean PM at larger distances approaching (μ_l cos(b), μ_b) = (0, 0). Dotted lines indicate μ_l cos(b) = 0 mas yr^{-1}, $\mu_b = 0$ mas yr^{-1}.

While they are not free parameters in our model, for simplicity in notation, we denote the disk DF parameters as $\theta_{\rm Disk}$.

While this disk model is quite simple, we find that this model is effective at identifying stars in our sample that are disk-like (see Section 4.3). These stars are more likely to have higher proper motions, brighter apparent magnitudes, redder colors, and heliocentric LOS velocities closer to 0 km s^{-1}.

3.2. Halo Model

For the halo distribution, we work in spherical coordinates. We assume the broken halo density profile derived in Deason et al. (2011), with break radius $r_b = 27$ kpc and slopes $\alpha_{\rm in} = 2.3$, and $\alpha_{\rm out} = 4.6$. The probability that a star has a distance D_i given the density profile is given by:

$$p(D_i|\rho, l, b) \propto \rho(r_q(D_i, l, b)) \times D_i^2, \quad (4)$$

where the factor of D_i^2 arises from the spatial volume element in spherical coordinates.

We assume independent Gaussian velocity distributions for the three spherical components of motion, and assume $\langle v_r\rangle = \langle v_\theta\rangle = 0$ km s^{-1}. We define our vector of halo ellipsoid parameters to be $\theta_{\rm Halo} = \{\langle v_\phi\rangle, \sigma_r, \sigma_\phi, \sigma_\theta\}$. We denote the joint velocity PDF:

$$\begin{aligned} F_{v,\rm Halo}(v_{r,i}, v_{\phi,i}, v_{\theta,i}) = & N(v_{r,i}|0, \sigma_r^2 + \sigma_{v_r,i}^2) \\ & \times N(v_{\phi,i}|\langle v_\phi\rangle, \sigma_\phi^2 + \sigma_{v_\phi,i}^2) \\ & \times N(v_{\theta,i}|0, \sigma_\theta^2 + \sigma_{v_\theta,i}^2), \end{aligned} \quad (5)$$

where $v_{r,i}$, $v_{\phi,i}$, $v_{\theta,i}$ are the Galactocentric velocities corresponding to data y_i and distance D_i. The corresponding uncertainties on these velocities are denoted by $\sigma_{v_r,i}^2$, $\sigma_{v_\phi,i}^2$, $\sigma_{v_\theta,i}^2$. Proper motions in Galactic coordinates are converted to physical velocities using the fact that tangential velocity is proportional to distance: $v_T = 4.74047\,\mu D$, where μ is the proper motion in mas yr^{-1} and D is in kpc. Tangential velocities are converted to the Galactocentric frame by correcting for the projection of the Sun's velocity along a given line of sight. We convert ($v_{\rm LOS}$, v_l, v_b) to spherical coordinates (v_r, v_ϕ, v_θ) by assuming a circular speed of 240 km s^{-1} at the position of the Sun ($R_0 = 8.5$ kpc), with solar peculiar motion (U, V, W) = (11.1, 12.24, 7.25) km s^{-1} (Schönrich et al. 2010).

We note that, in order to evaluate the probability of $\theta_{\rm Halo}$ given our observables, we need to consider the Jacobian matrix

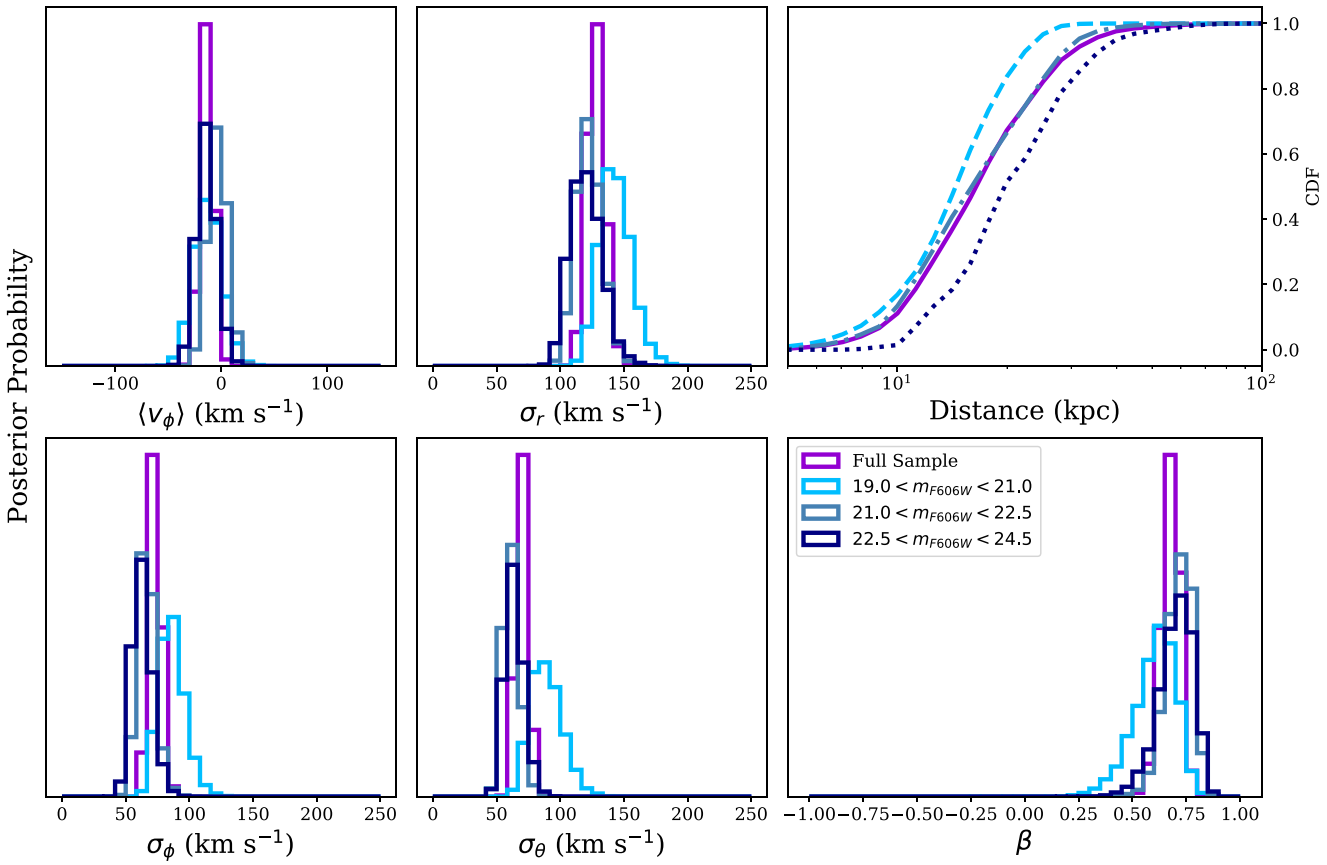

Figure 6. Summary of posterior results for spherically averaged samples. Left-hand panels: histograms of marginalized posterior samples for the four parameters of the halo velocity ellipsoid. Each of the estimates shown combines targets from all four survey fields. The estimates using the full HALO7D sample are shown in purple, while the blue histograms show the resulting estimates from three apparent magnitude bins. Upper right-hand panel: CDFs of the distances of the full sample and the three apparent magnitude bins. Lower right-hand panel: posterior distributions for β.

from the coordinate transformation from the observed frame to the Galactocentric frame:

$$p(y_i|D_i,\, \theta_{\rm Halo}) \propto F_{v,{\rm Halo}} \times D_i^2 \cos b, \tag{6}$$

where the factor of $D_i^2 \cos b$ arises due to the change in variables.

3.3. Absolute Magnitudes

Finally, as in Deason et al. (2013b), Cunningham et al. (2016), and in Paper I, we additionally constrain the absolute magnitude to a given star $M_{{\rm F814W},i}$ using information on its $m_{\rm F606W} - m_{\rm F814W}$ color.

We weight VandenBerg et al. (2006) isochrones in the *HST* filters according to the approximate age and metallicity distributions of the MW halo. We then generate a KDE to get the probability distribution function $G(M_{\rm F814W}|m_{{\rm F606W},i},\, m_{{\rm F814W},i})$.

3.4. Full Posterior

We now summarize how we sample from our full posterior distribution, for our parameters $\theta_{\rm Halo}$, $\boldsymbol{M}, \boldsymbol{f}$ given observables $\boldsymbol{y}, \boldsymbol{x}$. We can write down the likelihood under this model for a star with data y_i, explanatory variables $x_i = \{m_{{\rm F606W},i},\, m_{{\rm F814W},i},\, l_k,\, b_k\}$, given our model parameters:

$$\begin{aligned} &p(y_i|\theta_{\rm Halo},\, M_{{\rm F814W},i},\, f_{{\rm Disk},k}\,,\, x_i) \\ &= p(M_{{\rm F814W},i}|m_{{\rm F606W},i},\, m_{{\rm F814W},i}) \times D_i \\ &\times [f_{{\rm Disk},k} \times p(y_i|\theta_{\rm Disk},\, D_i) p(D_i|\rho_{\rm Disk},\, l_k,\, b_k) \\ &+ (1 - f_{{\rm Disk},k}) \times p(y_i|\theta_{\rm Halo},\, D_i) p(D_i|\rho_{\rm Halo},\, l_k,\, b_k)]. \end{aligned} \tag{7}$$

The extra factor of D_i arises due to the change of variables from absolute magnitude to distance: $M_{\rm F814W} \propto \log(D)$. The full likelihood, using stars from $k = 1, \ldots, K$ fields containing $N_{*,k}$ stars, is given by the product of the likelihoods of each individual data point:

$$\begin{aligned} &p(\boldsymbol{y}|\theta_{\rm Halo},\, \boldsymbol{M}, \boldsymbol{f}, \boldsymbol{x}) \\ &= \prod_{k=0}^{K} \prod_{i=0}^{N_{*,k}} p(y_i|\theta_{\rm Halo},\, M_{{\rm F814W},i},\, f_{{\rm Disk},k}\,,\, x_i). \end{aligned} \tag{8}$$

Likelihood in hand, we can write down the posterior distribution for our model parameters using Bayes' Theorem:

$$p(\theta_{\rm Halo},\, \boldsymbol{M}, \boldsymbol{f}|\boldsymbol{y}) \propto p(\boldsymbol{y},\, \boldsymbol{M}|\theta_{\rm Halo}, \boldsymbol{f}) \times p(\theta_{\rm Halo}, \boldsymbol{f}), \tag{9}$$

where $p(\theta_{\rm Halo},\, \boldsymbol{M}, \boldsymbol{f})$ is the prior distribution on model parameters. We assume standard reference priors on $\theta_{\rm Halo}$ (i.e., Jeffreys priors: $p(\langle v_\phi \rangle) \propto$ const and $p(\sigma) \propto 1/\sigma$ for all dispersions). We assume uniform priors on the $f_{\rm Disk}$ parameters ($p(f_{{\rm Disk},k}) = 1, f_{{\rm Disk},k}\, \epsilon\, [0,\, 1]$).

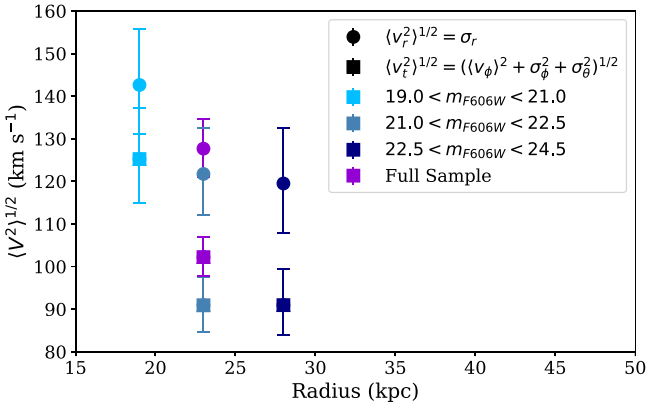

Figure 7. Square roots of the second moments of the radial (circular points) and tangential (square points) velocity distributions, as a function of mean Galactocentric radius. Different colors indicate the results from the analysis of the full sample (purple) as well as the three apparent magnitude bins (same colors as in Figure 6).

In order to sample for our model posterior parameters, we compute Equation (9) over a grid in absolute magnitude for every star. We then use `emcee` (Foreman-Mackey et al. 2013) to sample from our full posterior, marginalizing over the absolute magnitude of every star in each step of the chain. We test this modeling procedure on fake data; for details on how we generated fake data and tested our model, we refer the reader to Appendix C.

4. Results

In this section, we present posterior distributions for the halo velocity ellipsoid parameters. We first present the results using the full HALO7D sample, and then split our sample into three apparent magnitude bins. Finally, we consider the samples from each field separately. A summary of our results can be found in Table 3.

4.1. Spherically Averaged Estimates

We first estimate the parameters of the velocity ellipsoid using the full HALO7D sample of 188 stars. The parameters in this model are: the four ellipsoid parameters, the disk contamination in each of the four fields, and the absolute magnitude (and therefore distances) to each star. The resulting 1D marginalized distributions for the ellipsoid parameters are shown as the purple histograms in Figure 6. The left-hand panels show histograms of posterior samples for the four halo velocity ellipsoid parameters $\theta_{\rm Halo} = \{\langle v_\phi \rangle, \sigma_r, \sigma_\phi, \sigma_\theta\}$. Using the full sample of stars, we do not see a strong signature of halo rotation ($\langle v_\phi \rangle = -13 \pm 6$ km s^{-1}). We use the posterior samples of the ellipsoid parameters to derive a posterior estimate for the velocity anisotropy β; the resulting posterior distribution is shown as the purple histogram in the lower right-hand panel of Figure 6. We find that β is radially biased: at our mean sample distance of $\langle r \rangle = 23$ kpc, $\beta = 0.68^{+0.04}_{-0.05}$, consistent with estimates of β in the solar neighborhood (e.g., Bond et al. 2010).

In addition to modeling the full sample of stars, we also split our sample into three apparent magnitude bins. Because our distance estimates to each individual star are uncertain and probabilistic, we cannot divide our sample into different radial ranges; we therefore split the sample in apparent magnitude to study the radial variation of β. The resulting marginalized posterior distributions for the three apparent magnitude bins are shown as the blue histograms in Figure 6. Estimates using stars with $19.0 < m_{\rm F606W} < 21.0$ are shown in light blue; the estimates from stars with $21.0 < m_{\rm F606W} < 22.5$ are shown as gray blue; and $22.5 < m_{\rm F606W} < 24.5$ are shown in dark blue. The cumulative distribution functions (CDFs) for the distances to each of the three samples are shown in the upper right-hand corner of Figure 6, along with the CDF for distance of the full sample.

Figure 7 shows the second moments of the velocity distributions as a function of the average Galactocentric distance to the sample. We see a trend of decreasing velocity dispersion with distance, in both tangential and radial motion. However, when we compute the posterior distribution for β (blue histograms in lower right-hand panel of Figure 6), we find that all three estimates are consistent with the estimate of β from the full sample: β is radially biased for all of our spherically averaged samples.

4.2. Individual Fields

In the case of modeling fields individually, the free parameters in our model include the velocity ellipsoid parameters, the distance to each star in the field, and the fraction of disk contamination in the field.

Posterior samples for the ellipsoid parameters in each of the four fields are shown in Figure 8. The left-hand panels show histograms of posterior samples for the four halo velocity ellipsoid parameters $\theta_{\rm Halo} = \langle v_\phi \rangle$, σ_r, σ_ϕ, σ_θ. The upper right-hand panel shows the cumulative distribution for the distances to the four fields, and the lower right-hand panel shows the resulting posterior distribution for the velocity anisotropy.

When the four fields are treated separately, we see variation in the estimates of the velocity ellipsoid parameters. While the PDFs for GOODS-S are the broadest, because it has the smallest sample size, the GOODS-S distribution also shows a signature of rotation ($\langle v_\phi \rangle = -40^{+18}_{-17}$ km s^{-1}). The resulting estimate for β is consistent with isotropy, though also very broad, due in part to the small sample size in this field—but also due to the fact that circular orbits correspond to $\beta = -\infty$. In contrast, the estimates in the EGS field show no rotation, and the resulting estimate of β is strongly radially biased ($\beta_{\rm EGS} = 0.77^{+0.05}_{-0.06}$).

4.3. Disk Contamination

The marginalized 1D posterior distributions for the disk contamination in each of the four HALO7D fields are shown in Figure 9. The posteriors for $f_{\rm Disk}$ when the fields are treated individually are the thick black histograms; the colored histograms show the estimates in a given field for the spherically averaged estimates.

Our estimates for disk contamination are low (on the order of or less than 10%); this is consistent with the predicted disk contamination levels predicted by the Besançon Galaxy Model (Robin et al. 2003; see Paper I). Because GOODS-N and GOODS-S have smaller sample sizes than EGS and COSMOS, their posterior distributions for $f_{\rm Disk}$ are broader, but the posterior modes are still around 10%. As is to be expected, the disk contamination is highest for the brightest apparent magnitude bin (light blue histograms).

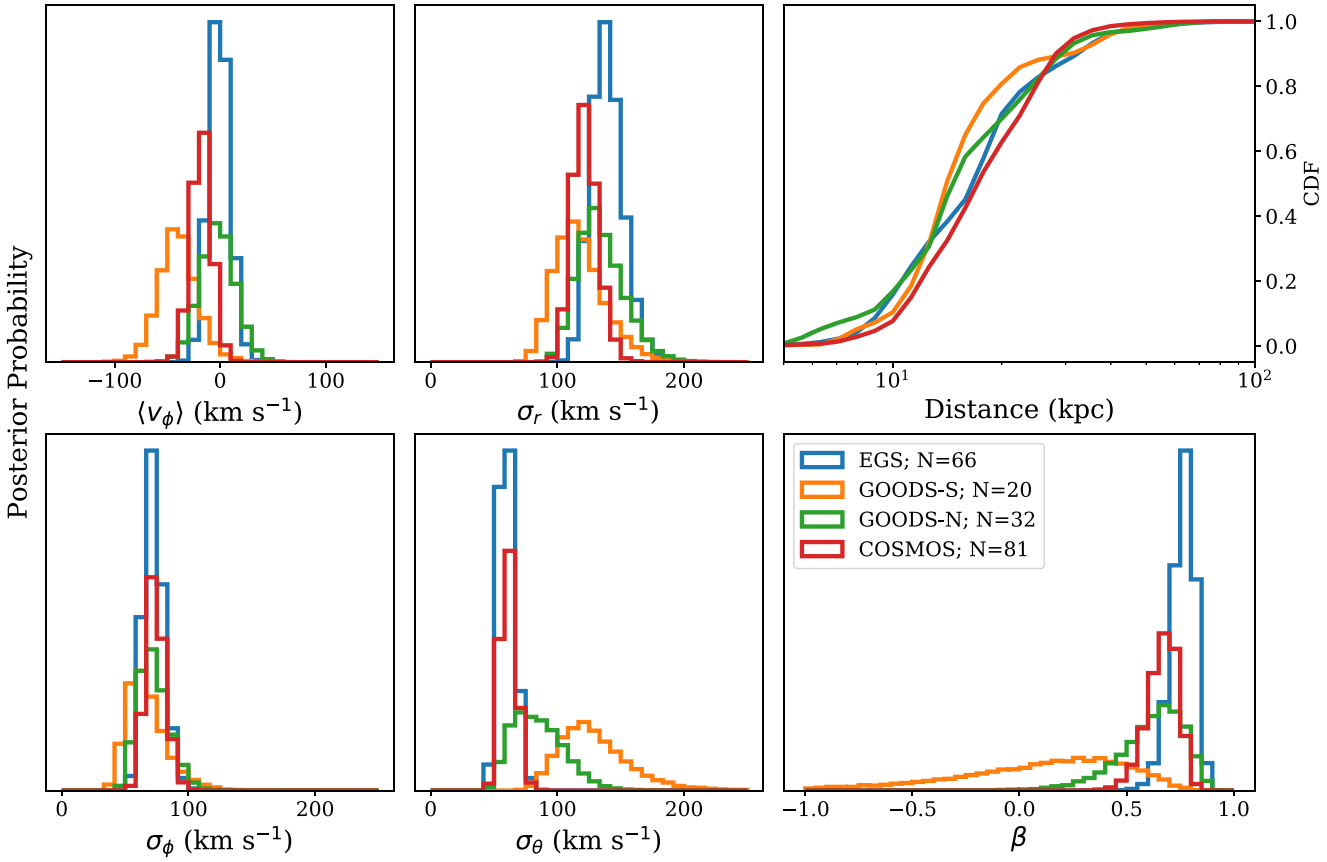

Figure 8. Summary of posterior results for the four fields. Left-hand panels: histograms of marginalized posterior samples for the four parameters of the halo velocity ellipsoid. Each colored histogram represents a different HALO7D field. Upper right-hand panel: CDFs for the distances of the stars in the four fields. Lower right-hand panel: posterior distributions for β.

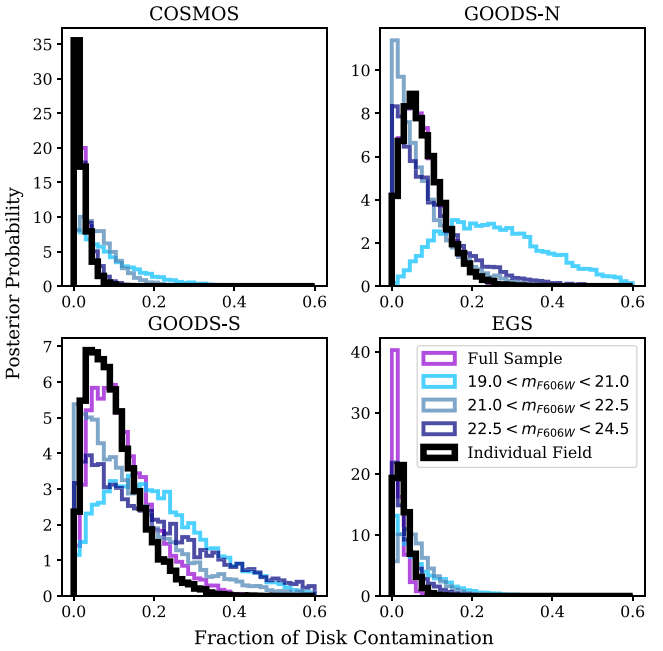

Figure 9. Posterior distributions for the disk contamination in the four HALO7D fields for each of the models. Black histograms indicate the posterior distributions for the fraction of disk stars when the fields are modeled individually. Colored histograms indicate the full sample (purple histograms) and the spherically averaged estimates in different apparent magnitude bins (as in Figures 6 and 7).

4.4. The β Radial Profile

Figure 10 summarizes all of our estimates of the velocity anisotropy, as a function of mean distance. Our spherically averaged estimates are plotted as circles, while the estimates of our individual fields are shown as squares. Gray points are results from other studies that used 3D kinematics to estimate β: gray triangles show the estimates of β from MW GCs, using PMs from both *HST* (Sohn et al. 2018) and *Gaia* (Watkins et al. 2019). The gray diamond shows the 3D estimate of β in the solar neighborhood from SDSS (Bond et al. 2010), and the gray square shows the C16 estimate of β along the line of sight toward M31. Gray crosses show the recent estimates of β from Lancaster et al. (2019) using *Gaia* DR2 PMs of blue horizontal branch stars.

Our spherically averaged estimates of β, which find radially biased $\beta \sim 0.6$–0.7, are consistent with one another and with other studies that have estimated β averaging over different parts of the sky. However, our field-to-field estimates (including the estimate from C16) show substantial variation, from strongly radially biased (EGS) to isotropic (GOODS-S) to mildly tangentially biased (M31). While the GOODS-S and M31 fields each have lower posterior estimates for β, these two fields also have the smallest sample size. Because of the way β is defined, estimates of β are sensitive to sample size and measurement uncertainties. We therefore assess how much our sample size should concern us, by testing fake data. We generate 100 fake data sets (in the method described in Appendix C), from velocity

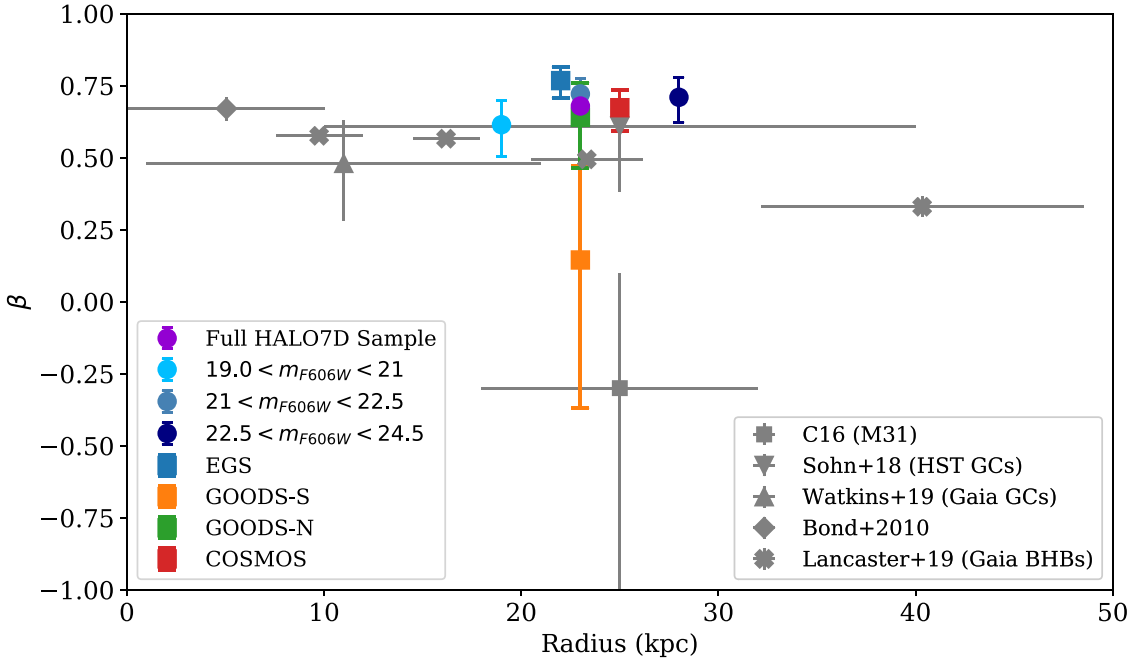

Figure 10. The Milky Way's radial anisotropy profile, β, as measured from 3D kinematics. Colored points indicate results from this work, while gray points indicate findings from previous work and other studies. The gray diamond shows the anisotropy estimate from Bond et al. (2010), using main-sequence stars from SDSS, and the gray square shows the estimate from Cunningham et al. (2016), using 13 MW MSTO stars along the line of sight toward M31. Gray crosses show the estimates of β from Lancaster et al. (2019), using the overall estimate of β consisting of the mixture of a metal-rich, radially biased population and an isotropic, metal-poor population, from BHBs in *Gaia* DR2. The two recent estimates for β from MW globular clusters, using *HST* PMs and *Gaia* PMs, are shown with triangles (Sohn et al. 2018; Watkins et al. 2019). Square-shaped points are results from individual fields, while our spherically averaged results are shown as circles. When using small fields to estimate anisotropy, β varies from mildly tangential (e.g., GOODS-S, M31) to strongly radial (e.g., EGS). However, the spherically averaged estimates are all consistently $\beta \sim 0.6$ (and consistent with solar neighborhood and GC estimates), and the posterior means increase as a function of mean sample distance.

distributions that have $\beta_{\rm True} = 0.75$, each containing 20 stars. Out of the 100 tests, only one of the fake data sets had a posterior distribution for β with median $\beta_{\rm Med} \leqslant 0.14$ (for the full distribution of β posterior medians, see Figure 15 in Appendix C). We do not see small sample size resulting in a systematic underestimate of β. Therefore, while the small sample size does contribute to the large uncertainty on β in this field, based on our fake data testing, we do not expect that the observed isotropic β is purely due to sample size.

5. Comparison with Other Studies

In this paper, we use the HALO7D data set to estimate the parameters of the MW stellar halo velocity ellipsoid. We study the full HALO7D sample, the sample divided into three apparent magnitude bins, and the individual HALO7D fields. When averaging over the four HALO7D fields, we find consistent estimates for $\beta \sim 0.6$–0.7. Our spherically averaged results for β are consistent with results from other recent estimates of β using GCs as tracers (Sohn et al. 2018; Watkins et al. 2019). However, when we treat the four HALO7D fields separately, our estimates for the ellipsoid parameters, and thus β, show significant variation.

In their study of β profiles of simulated galaxies, Loebman et al. (2018) found that β profiles are generally increasingly radially biased as a function of radius. However, recently accreted material can cause short-lived (<0.2 Gyr) dips in the β profiles, and longer-lived (>0.2 Gyr) dips arise due to the disruption of the in situ stellar halo by the close passage of a massive satellite. These "dips" in the in situ stellar halo are more metal-rich than dips caused by the accreted stellar halo.

Several studies using LOS velocities alone have observed tangentially biased "dips" in the β profile (Sirko et al. 2004; Kafle et al. 2012; King et al. 2015); these dips occur approximately at the observed break in the MW density profile (Watkins et al. 2009; Deason et al. 2011; Sesar et al. 2011). The kinematic structure around the break radius $r_b \sim 27$ kpc is of interest in order to understand its origin. In their study of the Bullock & Johnston (2005) purely accreted stellar halos, Deason et al. (2013a) found that the buildup of stars at apocenter from a relatively early, massive accretion event, or a few synchronous events, can cause broken density profiles.

As pointed out by Hattori et al. (2017), studies of stars beyond $r \sim 15$ kpc using only LOS velocities are subject to underestimates of β. However, recent studies using *Gaia* PMs have found decreases in β around the break radius as well. Using blue horizontal branch stars in *Gaia* DR2, Lancaster et al. (2019) found that β decreases just beyond the break radius, from $\beta \sim 0.6$ at 20 kpc to $\beta \sim 0.4$ at 40 kpc (gray crosses in Figure 10). They argue that this is due to sharp decline in the fraction of stars belonging to a radially biased population that dominates the inner halo (i.e., the *Gaia*-Sausage) beyond its apocenter radius (which Deason et al. (2018) showed coincides with the MW break radius). Using LAMOST K-Giants with *Gaia* DR2 PMs, Bird et al. (2019) found strongly radially biased ($\beta \sim 0.8$) inside of $r \sim 25$ kpc, with β gradually decreasing beyond this radius, down to $\beta = 0.3$ at 100 kpc; however, Lancaster et al. (2019) also showed that the magnitude of the decrease observed in the Bird et al. (2019) study could be due to their treatment of measurement uncertainties.

When averaging over multiple fields, we do not see a dip in the β profile, nor a global decrease in β beyond the break

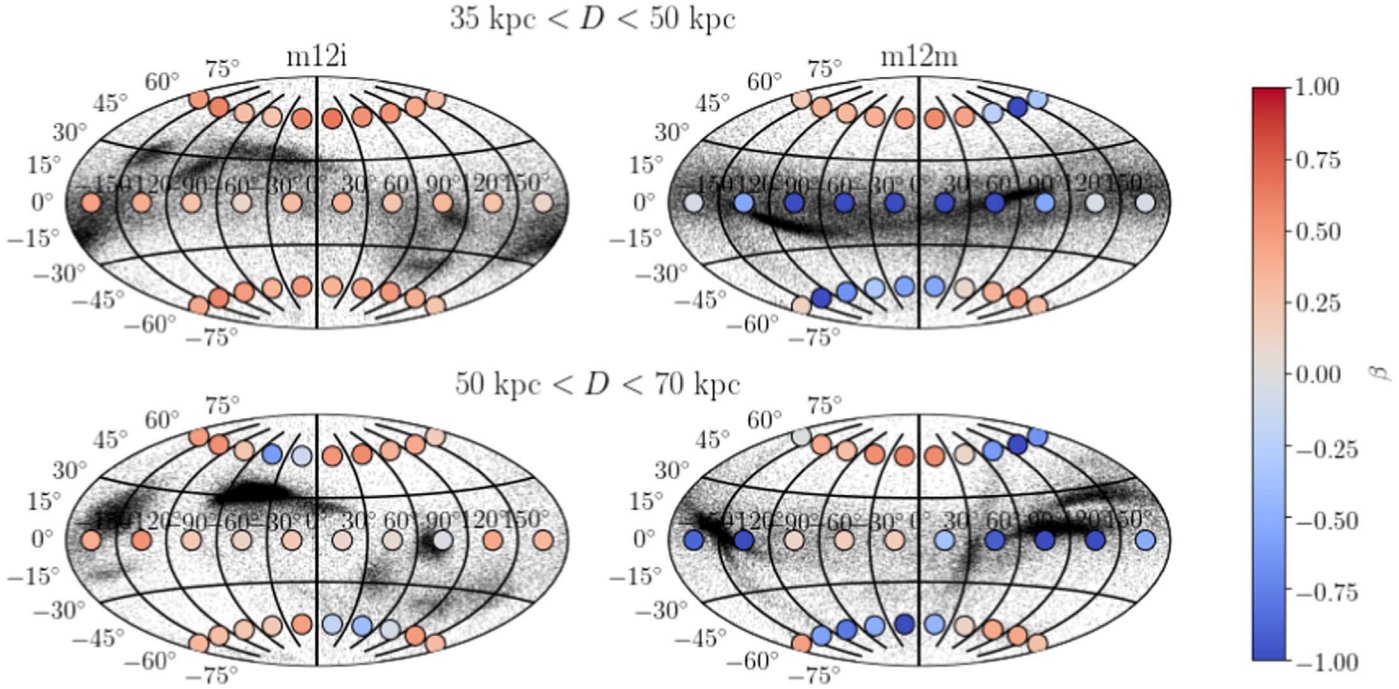

Figure 11. Maps of velocity anisotropy of the stellar halo in two *Latte* FIRE-2 simulations of Milky Way–mass galaxies: m12i (left) and m12m (right). The top panels show stars in the distance range 35 kpc $< D <$ 50 kpc, while the lower panels show 50 kpc $< D <$ 70 kpc. Black points show the positions of star particles in Galactic coordinates. In each halo, the sky has been subdivided into patches, and the color of the large circle in each patch indicates the velocity anisotropy for that subset of stars. Within a given distance range, each halo shows variation in its velocity anisotropy across the sky. Variation as a function of distance is also evident. In addition, the median and spread in β both vary from halo to halo: many more of the star particles in m12m are on tangentially biased orbits than in m12i.

radius. While our estimates are around the MW break radius, the posterior medians of our spherically averaged estimates are consistent with one another. Increasing β as a function of radius is predicted by simulations (e.g., Abadi et al. 2006; Sales et al. 2007; Rashkov et al. 2013; Loebman et al. 2018). However, we need to probe to larger distances beyond the break radius to see whether this prediction is consistent with the data or if β starts to decrease (as seen by Bird et al. (2019) and Lancaster et al. (2019)).

When we treat our different lines of sight separately, we see potential evidence for a dip in β toward GOODS-S and M31. Based on the Loebman et al. (2018) findings, these sightlines could be dominated by material that has been recently accreted or kicked up by the passage of Sagittarius. As discussed in the Introduction, several overdensities previously believed to be accreted structures now show evidence of a potential disk origin, having been kicked out of the disk due to the passage of Sagittarius (e.g., Price-Whelan et al. 2015; Bergemann et al. 2018; Laporte et al. 2018). One such overdensity discussed in those works is TriAnd, located along the line of sight toward M31, which is also the lowest latitude of the HALO7D fields.

Measuring abundances for stars in the HALO7D fields from their Keck spectra (K. A. McKinnon et al. 2019, in preparation) will help to distinguish between the kicked-up disk scenario and the recent accretion scenario as the origin for the observed "dips" in β in GOODS-S and M31. Chemical abundances will also help to assess the origin of the strongly radially biased β estimate in EGS ($\beta_{\rm EGS} \sim 0.8$). Belokurov et al. (2018) discovered the "*Gaia*-Sausage" as a metal-rich ([Fe/H] > -1.7), radially biased ($\beta \sim 0.9$) population in *Gaia* DR1. Given that the estimate of β in EGS is more radially biased than the estimates of β in the other fields, it is possible that the sample of stars in EGS is dominated by Sausage stars. Chemical abundances will be essential in assessing to what extent the Sausage is contributing to the HALO7D sample.

6. Comparison with Simulations

When we treat the four HALO7D fields separately, we see variation in the estimates of the velocity ellipsoid parameters (and the resulting velocity anisotropy). In this section, we explore the spatial variation of velocity anisotropy in two halos from the *Latte* suite of FIRE-2 cosmological zoom-in baryonic simulations of Milky Way–mass galaxies (introduced in Wetzel et al. (2016)), part of the Feedback In Realistic Environments (FIRE) simulation project.[9] These simulations were run using the Gizmo gravity plus hydrodynamics code in meshless finite-mass (MFM) mode (Hopkins 2015) and the FIRE-2 physics model (Hopkins et al. 2018). In this work, we discuss halos m12i (initially presented in Wetzel et al. (2016)) and m12m (initially presented in Hopkins et al. (2018)), making use of the publicly available $z = 0$ snapshots (Sanderson et al. 2018b).[10] The properties of the halos of these galaxies have been shown to agree reasonably well with the properties of the MW and M31, including: the stellar-to-halo mass relation (Hopkins et al. 2018); satellite dwarf galaxy stellar masses, stellar velocity dispersion, metallicities, and star formation histories (Wetzel et al. 2016; Escala et al. 2018; Garrison-Kimmel et al. 2019); and stellar halos (Bonaca et al. 2017; Sanderson et al. 2018a). In particular, the high resolution of the *Latte* simulations (star particles have initial masses $m \approx 7000\,M_\odot$ and gravitational force softening of 4 pc) means that they resolve satellite dwarf galaxies down to $M_{\rm star} \gtrsim 10^5\,M_\odot$, thus resolving the galaxies that are expected to contribute the

[9] FIRE project website: http://fire.northwestern.edu.
[10] $z = 0$ snapshots available at http://ananke.hub.yt.

majority of mass to the formation of the stellar halos (e.g., Deason et al. 2015).

Despite the high resolution of the *Latte* simulations, at large distances in the halos, the typical spacing between star particles can be large compared to the sizes of the HALO7D fields (less than a square degree). Therefore, a detailed comparison of exactly how our selection effects, observational errors, and field sizes are affecting our results is beyond the scope of this work. In addition, such a comparison may be of limited usefulness, given that variation observed across areas as small as the HALO7D fields could be due to structures below the simulation resolution limit (i.e., debris from accreted satellites with $M_{\rm star} < 10^5\,M_\odot$). As a first step, we explore the spatial variation in the velocity anisotropy computed directly from the star particles in the simulation, using 30 larger fields, each spanning 36° in longitude and 60° in latitude.

Figure 11 shows the m12i simulation (left panels) and m12m (right panels). The top panels show the positions of star particles (black points), in Aitoff projection, within the distance range $35 < D < 50$ kpc; the lower panels show star particles in the distance range $50 < D < 70$ kpc. While these radial ranges are farther out than the HALO7D data, we choose these ranges to avoid the thick disks in these simulations, which are extended and kinematically hotter than the MW (Sanderson et al. 2018b; S. R. Loebman et al. 2019, in preparation). Star particle positions are plotted in Galactic coordinates. Galactocentric frames are defined in the method described in Section 3 of Sanderson et al. (2018b), and positions are converted to Galactic coordinates using the `astropy.coordinates` package (Astropy Collaboration et al. 2013; Astropy Collaboration et al. 2018). We use the default options in `astropy.coordinates` for the position of the Sun ($R_\odot = 8.3$ kpc; Gillessen et al. 2009). The "sky" in each halo has been divided into patches, and the resulting velocity anisotropy computed from the star particles in each patch is shown by the colored points. We note that we compute the velocity anisotropy using all the star particles within a given area on the sky and radial range; we do not exclude particles in bound satellite galaxies. This choice likely affects the resulting β maps, and we plan to explore the effects of excluding and including bound satellites on β estimates in future work.

The velocity anisotropy β shows variation across the sky of a given halo, as well as with radius. In addition, these maps of velocity anisotropy are very different across the two halos: within $35 < D < 50$ kpc, all patches in m12i are radially biased, but many of the patches of m12m are tangentially biased β. At $50 < D < 70$ kpc, both m12i and m12m show some tangentially biased patches and radially biased patches. The overall means and spreads of β values measured across the two halos are quite different: m12i has a mildly radially biased $\langle\beta\rangle \sim 0.3$ with a standard deviation of 0.2, whereas m12m has tangentially biased $\langle\beta\rangle \sim -0.3$ with a standard deviation of 0.7. The magnitude of the β variation observed in these two simulated galaxies is very similar to the range of β values measured across the HALO7D fields; in both Figures 10 and 11, we see variation in β over the range of $[-1, 1]$.

The differences in the β maps across these two halos are likely linked to their different accretion histories. Over these radial ranges in the simulated halos, the majority of the material mapped in Figure 11 is accreted, and the accreted debris in the two halos have visibly different spatial and kinematic properties. We intend to explore in future work what characteristics of a galaxy's accretion history, such as accretion times, initial orbital conditions, and masses of accreted satellites, are primarily responsible for the observed β variation patterns. Based on the Loebman et al. (2018) findings, patches with tangentially biased β could indicate recently accreted material. Further study of the accretion histories of these simulated galaxies will help us to understand what accretion events and accretion histories give rise to different β variation patterns in galaxy halos, as well as what characteristics of the MW's assembly history we might be able to constrain through mapping its spatial β variation.

The β variation we observe in HALO7D and the *Latte* simulations also could have implications for the validity of MW mass estimates derived from Jeans modeling. The fundamental assumption underlying Jeans modeling is that the tracers are virialized and in dynamical equilibrium. The spatial maps and β variation observed in the Latte halos reveal that this assumption is clearly violated in the simulations. The variation in β observed with HALO7D indicates that this assumption is invalid in the MW halo as well; our results are evidence that the halo is not phase-mixed at $\langle r\rangle \sim 23$ kpc. Just how significantly the violation of the assumption of dynamical equilibrium will affect estimates of the MW mass remains to be determined. The systematic uncertainty of traditional spherical Jeans mass modeling in recovering halo masses has been observed in a number of simulations (e.g., Eadie et al. 2018; Kafle et al. 2018; Wang et al. 2018); we leave the full characterization of the effects of β variation on different approaches of MW mass estimates on the *Latte* halos to future work.

7. Conclusions

In this paper, we present the proper motions of distant, main-sequence turnoff MW halo star candidates as measured with *HST*. These PMs are measured as a part of the HALO7D project, and have LOS velocities measured from Keck spectroscopy (Paper I). Using the 3D kinematic sample from HALO7D, we estimate the parameters of the halo velocity ellipsoid and velocity anisotropy. We estimate these parameters treating the individual survey fields separately, as well as spherically averaging over all fields. We summarize our main results as follows:

1. Using the full HALO7D sample of 188 stars, we estimate the velocity anisotropy $\beta = 0.68^{+0.04}_{-0.05}$ at $\langle r\rangle = 23$ kpc. This estimate is consistent with other recent estimates of β.
2. We estimate β from the HALO7D sample split into three apparent magnitude bins to explore the radial dependence. While estimates of velocity dispersions decrease as a function of mean sample distance, the overall estimates of β are consistent across apparent magnitude bins. Posterior medians increase as a function of mean sample distance, consistent with predictions from simulations.
3. When we treat our stars from the four HALO7D fields separately, estimates of the halo velocity ellipsoid parameters show variation from field-to field. This variation could be evidence for recent accretion; it is also possible that the isotropic and tangentially biased β values from GOODS-S and M31 (respectively) are due to the presence of kicked-up disk stars. The observed

variation in β is evidence that the halo is not phase-mixed at $r \sim 23$ kpc.

4. We map the velocity anisotropy in two stellar halos from the *Latte* suite of FIRE-2 simulations and see variation in β across the skies of these two halos over a similar range to the variations observed in the HALO7D fields. In the simulated galaxies, the degree of—and patterns in—these variations are clearly tied to their different accretion histories. A more detailed study of the full accretion histories of these galaxies will shed light on the types of signatures that different accretion events can leave in β maps.

Fortunately, many of the questions raised in this work will be answerable in the near future. Abundances from HALO7D spectra will provide key insights as to the origin of the observed β variation. In addition, β variation in the MW can be mapped with the *Gaia* data set, and ultimately, LSST. Thanks to the quality of current and upcoming data, coupled with high-resolution cosmological hydrodynamical simulations, we are rapidly progressing in our knowledge of our Galaxy's structure and formation.

We would like to thank the anonymous referee for helpful comments and suggestions. E.C.C. would like to thank Evan Kirby, Zachary Jennings, and Lachlan Lancaster for their helpful comments, and Lachlan Lancaster for providing his data for Figure 10. Over the course of this work, E.C.C. was supported by an NSF Graduate Research Fellowship and an ARCS Foundation Fellowship, as well as NSF Grant AST-1616540. Partial support for this work was provided by NASA through grants for program AR-13272 from the Space Telescope Science Institute (STScI), which is operated by the Association of Universities for Research in Astronomy (AURA), Inc., under NASA contract NAS5-26555. A.D. is supported by a Royal Society University Research Fellowship. A.D. also acknowledges support from the STFC grant ST/P000451/1. A.W. was supported by NASA through ATP grant 80NSSC18K1097 and grants *HST*-GO-14734 and *HST*-AR-15057 from STScI. S.L. was supported by NASA through Hubble Fellowship grant #*HST*-JF2-51395.001-A awarded by the Space Telescope Science Institute, which is operated by the Association of Universities for Research in Astronomy, Inc., for NASA, under contract NAS5-26555. This project was carried out in the context of, and used software created by, the HSTPROMO (High-resolution Space Telescope PROper MOtion) Collaboration.[11] This research made use of Astropy, a community-developed core Python package for Astronomy (Astropy Collaboration et al. 2013; Astropy Collaboration et al. 2018). This work has made use of data from the European Space Agency (ESA) mission *Gaia* (https://www.cosmos.esa.int/gaia), processed by the *Gaia* Data Processing and Analysis Consortium (DPAC, https://www.cosmos.esa.int/web/gaia/dpac/consortium). Funding for the DPAC has been provided by national institutions, particularly the institutions participating in the *Gaia* Multilateral Agreement. This work has made use of the Rainbow Cosmological Surveys Database, which is operated by the Universidad Complutense de Madrid (UCM), partnered with the University of California Observatories at Santa Cruz (UCO/Lick, UCSC). We recognize and acknowledge the significant cultural role and reverence that the summit of Maunakea has always had within the indigenous Hawaiian community. We are most fortunate to have the opportunity to conduct observations from this mountain.

[11] http://www.stsci.edu/~marel/hstpromo.html

Appendix

In this appendix, we provide the details of the Bayesian mixture model used to derive estimates of PMs. We first describe our model in Appendix B, and then the Gibbs sampling algorithm used to sample from the posterior distribution for model parameters in Appendix B.2.

Appendix A
Proper Motion Model

To map one image onto another, we perform a six-parameter linear transformation:

$$\begin{pmatrix} A & B & x_t - \delta u \\ C & D & y_t - \delta v \\ 0 & 0 & 1 \end{pmatrix} \begin{pmatrix} u \\ v \\ 1 \end{pmatrix} = \begin{pmatrix} u_{\rm ref} \\ v_{\rm ref} \\ 1 \end{pmatrix}, \tag{10}$$

where δu, δv represent the change (in pixels) of a star from one image to another due to proper motion (so, for galaxies, $\delta u = \delta v = 0$).

In our model, we treat stars and galaxies separately. For stars:

$$\begin{aligned} Au + Bv + x_t - \delta u &\sim N(u_{\rm ref}, \sigma_*^2) \\ Cu + Dv + y_t - \delta v &\sim N(v_{\rm ref}, \sigma_*^2) \\ u_{imref}, v_{imref} &\sim N(u_{\rm ref}, v_{\rm ref}, \sigma_*^2), \end{aligned} \tag{11}$$

where u_{imref}, v_{imref} are the measured positions in the defined reference image, whereas $u_{\rm ref}$, $v_{\rm ref}$ are the positions of the object in the reference epoch, which are free parameters. Because stars' central positions are measured well, we define $\sigma_* = 0.02$ pixels. Here, δu, δv represent the shift in pixels from image 1 to image 2, which can be converted to proper motions north and west, respectively:

$$\text{PMN} = \frac{\delta u \times 50 \text{ mas/pix}}{\Delta t}; \tag{12}$$

$$\text{PMW} = \frac{\delta v \times 50 \text{ mas/pix}}{\Delta t}, \tag{13}$$

where Δt is measured in years. We describe the galaxy positions as a two-component Gaussian mixture model. Defining a fixed location in an image as the galaxy's precise position is not trivial and sometimes fails, given that galaxies are resolved sources with complex morphologies. We therefore consider "good" galaxies (i.e., galaxies with well-measured positions) and "bad" galaxies (galaxies with poorly measured positions)

$$\begin{aligned} Au + Bv + x_t &\sim N(u_{\rm ref}, \sigma^2) \\ Cu + Dv + y_t &\sim N(v_{\rm ref}, \sigma^2) \\ u_{imref}, v_{imref} &\sim N(u_{\rm ref}, v_{\rm ref}, \sigma^2). \end{aligned} \tag{14}$$

For "good" galaxies, $\sigma = 0.1$ pixels, whereas for "bad" galaxies, $\sigma = 3$ pixels.

An example of the initial classification of "good" and "bad" galaxies is shown in Figure 12. Figure 12 shows the change in

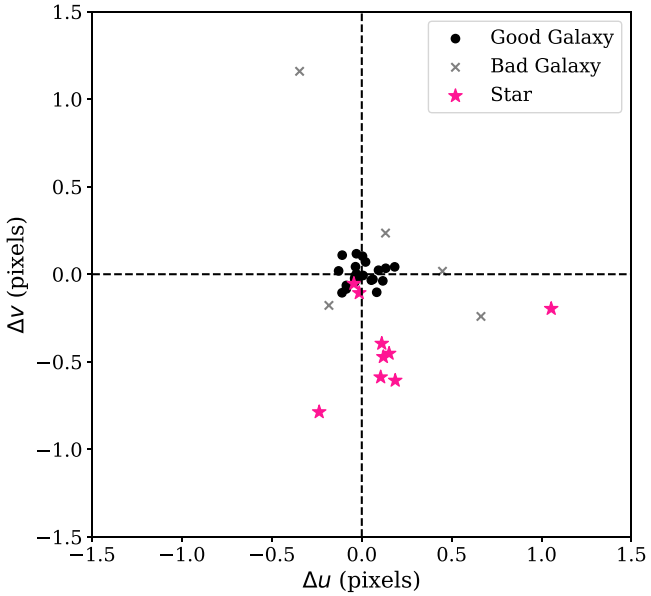

Figure 12. An example of the linear transformation method on two images, j8pu44cvq (taken in 2004) and jboa38c2q (from 2011). Axes represent the change in pixels, in the distortion-corrected frame (u, v), for objects in the two images, after applying the six-parameter linear transformation. Gray crosses indicate the change in positions for the galaxies initially classified as "bad;" black points are the positions of "good" galaxies used in the reference frame. The changes in positions of the "good" galaxies are clustered at (0, 0). Pink stars show change in the positions of the stars in these two images.

positions in pixels, in the distortion-corrected frame, for objects in two *HST* images, taken seven years apart. Black points show the positions of galaxies initially classified as "good;" these are clustered at (0, 0) because they were used in the reference frame for the linear transformation. Positions of galaxies initially classified as "bad" are shown as gray crosses. In our Bayesian mixture model, we allow galaxies to move in and out of the reference frame probabilistically. Pink points show the change in the positions of the stars in the images. These stars have a mean motion and scatter relative to the stationary reference frame of distant galaxies; these relate to the dynamical quantities of interest estimated in this study.

A.1. Gaussian Mixture Models Written with Indicator Variables

Mixture models can be expressed in different ways. For a two-component mixture model, the likelihood of a given data point can be written as

$$p(x|\theta) = \lambda N(x|\theta_1, \sigma_1^2) + (1 - \lambda)N(x|\theta_2, \sigma_2^2). \quad (15)$$

Here, λ is the fraction of objects in the underlying population that belong to distribution 1. However, sums in probability calculations make posterior sampling more difficult. To improve our sampling efficiency, we can rewrite the above equation using indicators z_j:

$$p(x, z|\theta) = (\lambda N(x|\theta_1, \sigma_1^2))^{z_1}((1 - \lambda)N(x|\theta_2, \sigma_2^2))^{z_2}. \quad (16)$$

In this construction, for a given step in the MCMC chain, the indicator $z_{ih} = 1$ if data point x_i is associated with component h, and $z_{ih} = 0$ otherwise.

Our full posterior thus takes the form:

$$\begin{aligned} &p(\theta|u_1 \ldots u_k,\ v_1 \ldots v_k,\ u_{im\mathrm{ref}},\ v_{im\mathrm{ref}}) \\ &\propto \prod_{k=1}^{N_{im}} \prod_{j=1}^{N_{\mathrm{stars}}} \exp\left\{\frac{1}{2\sigma_*^2}(Au_{jk} + Bv_{jk} + x_{t,k} - \delta u_{jk} - u_{\mathrm{ref}})^2\right. \\ &\left. + \frac{1}{2\sigma_*^2}(Cu_{jk} + Dv_{jk} + y_{t,k} - \delta v_{jk} - v_{\mathrm{ref}})^2\right\} \\ &\times \prod_{j=1}^{N_{\mathrm{gals}}} \left(f_{g,k} \exp\left\{\frac{1}{2\sigma_g^2}(Au_{jk} + Bv_{jk} + x_{t,k} - u_{\mathrm{ref}})^2\right.\right. \\ &\left.\left. + \frac{1}{2\sigma_*^2}(Cu_{jk} + Dv_{jk} + y_{t,k} - v_{\mathrm{ref}})^2\right\}\right)^{z_{g,jk}} \\ &\times \left((1 - f_{g,k})\exp\left\{\frac{1}{2\sigma_b^2}(Au_{jk} + Bv_{jk} + x_{t,k} - u_{\mathrm{ref}})^2\right.\right. \\ &\left.\left. + \frac{1}{2\sigma_b^2}(Cu_{jk} + Dv_{jk} + y_{t,k} - v_{\mathrm{ref}})^2\right\}\right)^{z_{b,jk}} \end{aligned} \quad (17)$$

where $f_{g,k}$ is the fraction of good galaxies in image k, and z_{jg} is the indicator for galaxy j in image k. By construction, if a galaxy has a "good" position in image k, $z_{g,jk} = 1$ and $z_{b,jk} = 0$ (i.e., a galaxy can only belong to one mixture component at a time).

A.2. Gibbs Sampling Algorithm

To sample from the posterior distribution for our parameters, we use Gibbs sampling. In a Gibbs sampler, we sample directly from the conditional posterior distributions for each parameter. Gibbs samplers can only be used if the full conditional distributions of the parameters can be written in closed form, which is usually only the case when conjugate priors (or, in special cases, reference priors) have been used.

Our Gibbs sampling algorithm consists of the following steps:

1. Initialize the transformation parameters for each image using standard linear least squares. If the image is in the same epoch as the reference image, use the star positions to match frames. Otherwise, use the positions of the "good" galaxies. Initial values for PMs are averaged over the images, and initial values for the reference positions are those in the reference image.
2. For each star, we draw from the conditional posterior distributions for PMN and PMW, as well as the conditional posterior distributions for the reference positions. The conditional distributions for proper motions are:

$$\begin{aligned} \mathrm{PMW} \sim N\Bigg(&\frac{50\ \mathrm{mas/pix}}{k\sum \Delta t_k^2} \sum_{k=1}^{N_{im,k}} \delta u_k \\ &\times \Delta t_k,\ (50\ \mathrm{mas/pix})^2 \times \frac{\sigma_*^2}{\sum \Delta t^2}\Bigg) \end{aligned} \quad (18)$$

Table 4
Conditional Posterior Parameters for Image Transformations

Parameter	μ/V	V^{-1}
A	$\sum\frac{u_j \times u_{\mathrm{ref},j}}{\sigma_j^2} - B\sum\frac{u_j \times v_j}{\sigma_j^2} - x_t\sum\frac{u_j}{\sigma_j^2} + \sum\frac{\delta u_j u_j}{\sigma_j^2}$	$\sum\frac{u_j^2}{\sigma_j^2}$
B	$\sum\frac{v_j \times u_{\mathrm{ref},j}}{\sigma_j^2} - A\sum\frac{u_j \times v_j}{\sigma_j^2} - x_t\sum\frac{v_j}{\sigma_j^2} + \sum\frac{\delta u_j v_j}{\sigma_j^2}$	$\sum\frac{v_j^2}{\sigma_j^2}$
C	$\sum\frac{u_j \times v_{\mathrm{ref},j}}{\sigma_j^2} - D\sum\frac{u_j \times v_j}{\sigma_j^2} - y_t\sum\frac{u_j}{\sigma_j^2} + \sum\frac{\delta v_j u_j}{\sigma_j^2}$	$\sum\frac{u_j^2}{\sigma_j^2}$
D	$\sum\frac{v_j \times v_{\mathrm{ref},j}}{\sigma_j^2} - C\sum\frac{u_j \times v_j}{\sigma_j^2} - y_t\sum\frac{u_j}{\sigma_j^2} + \sum\frac{\delta v_j v_j}{\sigma_j^2}$	$\sum\frac{v_j^2}{\sigma_j^2}$
x_t	$A\sum\frac{u_j}{\sigma_j^2} + B\sum\frac{v_j}{\sigma_j^2}$	n_{obj}/σ_j^2
y_t	$C\sum\frac{u_j}{\sigma_j^2} + D\sum\frac{v_j}{\sigma_j^2}$	n_{obj}/σ_j^2

Note. Conditional posteriors for all six image transformation parameters are normal distributions with mean μ and variance V. Sums are over all objects in an image. Here, $\sigma_j = 0.02$ for stars, $\sigma_j = 0.1$ for "good" galaxies, and $\sigma_j = 3.$ for "bad" galaxies.

$$\mathrm{PMN} \sim N\left(\frac{50\ \mathrm{mas/pix}}{k\sum\Delta t_k^2}\sum_{k=1}^{N_{im,k}}\delta v_k \times \Delta t_k,\ (50\ \mathrm{mas/pix})^2 \times \frac{\sigma_*^2}{\sum\Delta t^2}\right). \quad (19)$$

3. For each galaxy, we first loop over each image, including the reference image, and draw an indicator. We allow a galaxy to be "good" in some subset of images and "bad" in another. We draw the indicator for a given galaxy as a Bernoulli variable with probability:

$$p = \frac{f_{\mathrm{gal}} \times N(u|u_{\mathrm{ref}}, \sigma_g^2) \times N(v|v_{\mathrm{ref}}, \sigma_g^2)}{f_{\mathrm{gal}} \times N(u|u_{\mathrm{ref}}, \sigma_g^2) \times N(v|v_{\mathrm{ref}}, \sigma_g^2) + (1 - f_{\mathrm{gal}}) \times N(u|u_{\mathrm{ref}}, \sigma_b^2) \times N(v|v_{\mathrm{ref}}, \sigma_b^2)}. \quad (20)$$

We then draw from the conditional posterior distributions for the reference frame positions of each object.

4. Finally, we loop over each image, drawing from the conditional posterior distributions for the image parameters (A, B, C, D, u_t, y_t, f_{gal}) (see Table 4). The f_{gal} parameters are drawn from beta distributions:

$$p(f_{\mathrm{gal},k}|...) \sim \mathrm{Beta}(n_{\mathrm{goodgals},k} + 1,\ n_{\mathrm{badgals},k} + 1) \quad (21)$$

where $n_{\mathrm{goodgals},k}$, $n_{\mathrm{badgals},k}$ are computed by summing the indicators for each population at that step in the chain.

Appendix B
Fake Data Testing for Ellipsoid Model

In this appendix, we discuss how we tested our method for estimating the parameters of the velocity ellipsoid using fake data. To create fake data for a given line of sight for this model, we perform the following operations.

1. Generate samples from our kernel density estimate for M_{F81W} versus $M_{\mathrm{F606W}} - M_{\mathrm{F814W}}$, based on the weighted VandenBerg et al. (2006) isochrones.
2. Assign each draw an apparent magnitude, drawn from a uniform distribution in m_{F814W} over the range [19, 24.5].
3. Given the resulting distances from the draws in apparent and absolute magnitudes, we use Monte Carlo acceptance/rejection to keep draws consistent with the MW density profile of Deason et al. (2011).
4. Assign stars velocities in spherical coordinates, based on random draws from normal distributions.
5. Convert D, V_r, V_ϕ, V_θ to μ_l, μ_b, v_{LOS} using the `astropy.coordinates` package. Given that we do not use `astropy.coordinates` to perform the velocity transformations in our ellipsoid modeling code, this step provides an additional check on our coordinate transformations.
6. Draw fake measured values from normal distributions centered on μ_l, μ_b, v_{LOS}, with dispersions corresponding to measurement uncertainties. For the purposes of this testing, we assign PM uncertainties of 0.2 mas yr^{-1} and LOS velocity uncertainties based on a fit of the relation between apparent magnitude and LOS velocity error shown in Figure 7 of Paper I.

We generate fake disk stars using a similar method, except drawing stars from the density profile and velocity distributions for our disk model. Figure 13 shows the posterior distribution for the halo ellipsoid parameters when our analysis is performed on a fake data set. This particular fake data set contains 100 halo star and 50 disk stars in the GOODS-N field. Values for the parameters used to generate the data are shown in blue.

Results from testing 30 fake halo data sets, each with 100 stars, are shown in Figure 14. Top panels show histograms of posterior medians for each simulated data set; bottom panels are histograms of the errors measured in each data set (computed as half the difference of the 84th and 16th percentiles). The errors in the posterior distributions are reasonable, given the observed spread in posterior medians. The resulting distribution of posterior medians for β are shown in the left-hand panel of Figure 15.

B.1. Sensitivity to Sample Size

In order to assess how the sample size of the GOODS-S field affects the estimate of β in that field, we generated 100 fake data sets, each containing 16 stars. These data sets were generated from velocity distributions that have $\beta_{\mathrm{True}} = 0.75$. Figure 15 shows the distribution of the resulting posterior medians for β when we model this fake data set. Out of the 100 fake data sets, only one had a posterior median with $\beta < 0.14$.

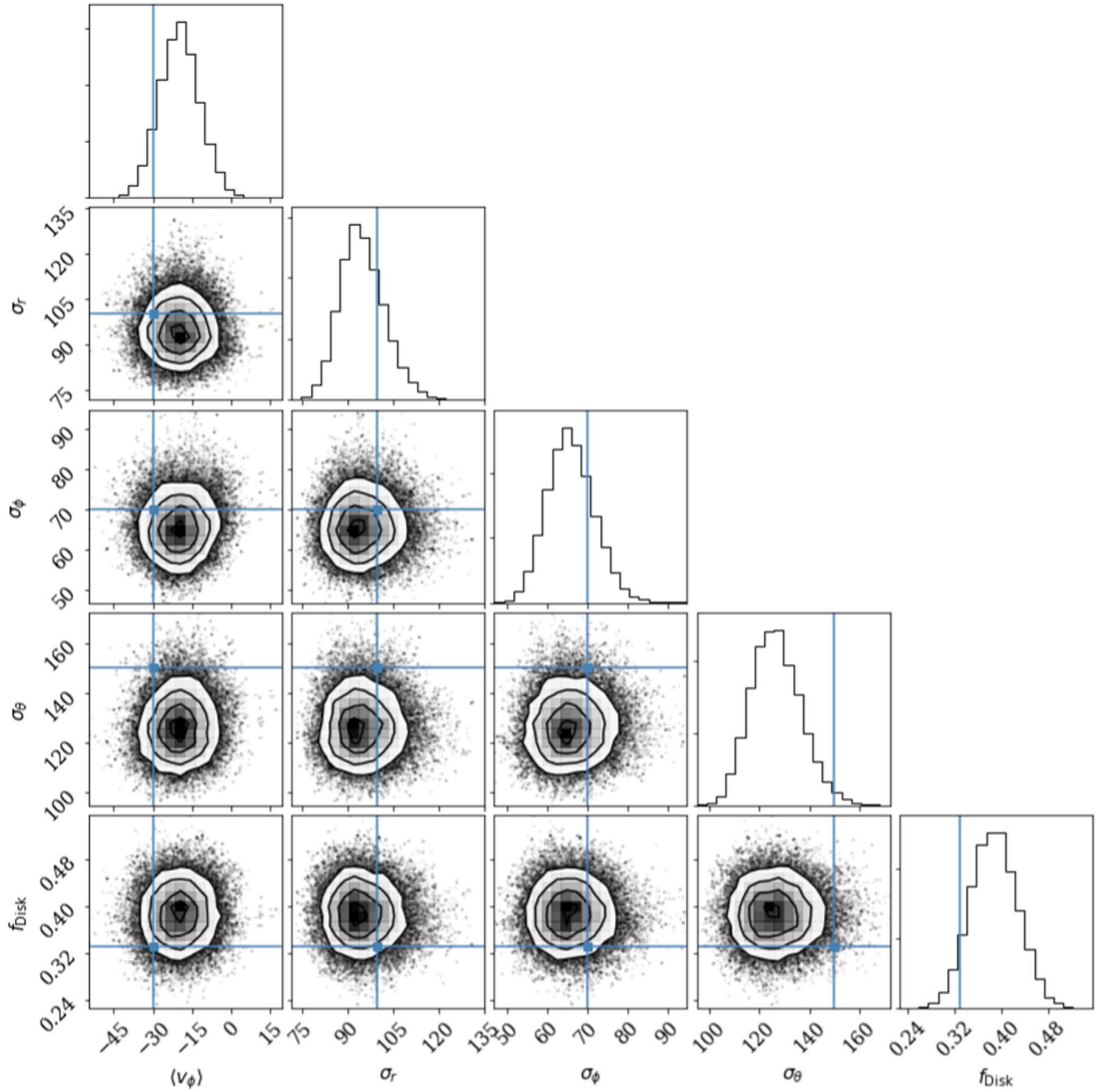

Figure 13. Resulting projections of posterior samples for fake GOODS-N data. This fake sample contained 100 halo stars and 50 disk stars. The true values of the distributions used to generate the data are shown in blue.

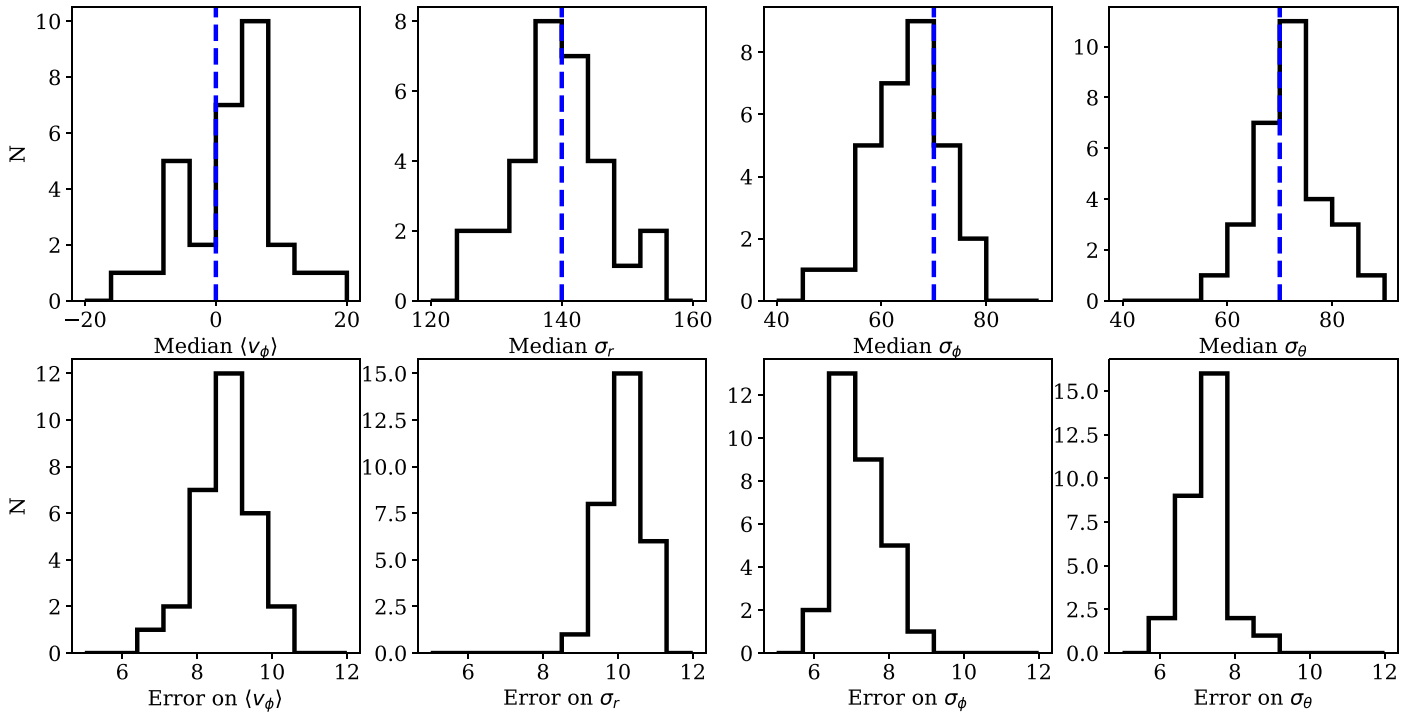

Figure 14. Top panel: distributions of posterior medians for the halo velocity ellipsoid parameters recovered from 30 fake data sets, each with 100 stars. Parameter values used to generate the fake data are shown as blue vertical dashed lines. Bottom panel: histograms of the the error estimates for each parameter.

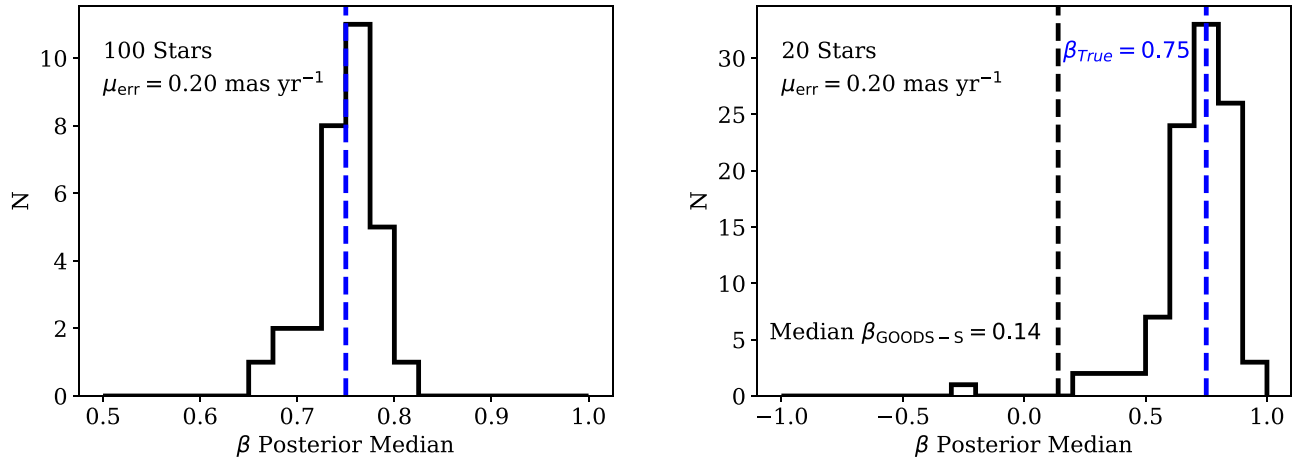

Figure 15. Histograms of posterior medians for the estimates of β from fake data testing. Left-hand panel: distribution of β estimates from 30 fake data sets, each containing 100 stars, with PM uncertainties of 0.2 mas yr^{-1}. Right-hand panel: the estimates of β from 100 fake data sets, each containing 20 stars, with PM errors of 0.20 mas yr^{-1}. For both sets of fake data sets, radial velocity uncertainties were assigned as a function of apparent magnitude (see Figure 7 of Paper I). None of the 100 fake data sets yielded a posterior median estimate of $\beta < 0.14$; the minimum posterior median estimate was $\beta_{min} = 0.20$.

ORCID iDs

Emily C. Cunningham https://orcid.org/0000-0002-6993-0826
Alis J. Deason https://orcid.org/0000-0001-6146-2645
Robyn E. Sanderson https://orcid.org/0000-0003-3939-3297
Sangmo Tony Sohn https://orcid.org/0000-0001-8368-0221
Jay Anderson https://orcid.org/0000-0003-2861-3995
Puragra Guhathakurta https://orcid.org/0000-0001-8867-4234
Roeland P. van der Marel https://orcid.org/0000-0001-7827-7825
Sarah R. Loebman https://orcid.org/0000-0003-3217-5967
Andrew Wetzel https://orcid.org/0000-0003-0603-8942

References

Abadi, M. G., Navarro, J. F., & Steinmetz, M. 2006, MNRAS, 365, 747
Anderson, J., & Bedin, L. R. 2010, PASP, 122, 1035
Anderson, J., & King, I. R. 2006, PSFs, Photometry, and Astronomy for the ACS/WFC, Tech. Rep., ACS 2006-01
Anderson, J., & van der Marel, R. P. 2010, ApJ, 710, 1032
Astropy Collaboration, Price-Whelan, A. M., Sipőcz, B. M., et al. 2018, AJ, 156, 123
Astropy Collaboration, Robitaille, T. P., Tollerud, E. J., et al. 2013, A&A, 558, A33
Belokurov, V., Erkal, D., Evans, N. W., Koposov, S. E., & Deason, A. J. 2018, MNRAS, 478, 611
Bergemann, M., Sesar, B., Cohen, J. G., et al. 2018, Natur, 555, 334

Binney, J. 2010, MNRAS, 401, 2318
Binney, J., & McMillan, P. 2011, MNRAS, 413, 1889
Binney, J., & Tremaine, S. 2008, Galactic Dynamics (2nd ed.; Princeton, NJ: Princeton Univ. Press)
Bird, S. A., Xue, X.-X., Liu, C., et al. 2019, AJ, 157, 104
Bonaca, A., Conroy, C., Wetzel, A., Hopkins, P. F., & Kereš, D. 2017, ApJ, 845, 101
Bond, N. A., Ivezić, Ž., Sesar, B., et al. 2010, ApJ, 716, 1
Bovy, J. 2015, ApJS, 216, 29
Bullock, J. S., & Johnston, K. V. 2005, ApJ, 635, 931
Cunningham, E. C., Deason, A. J., Guhathakurta, P., et al. 2016, ApJ, 820, 18
Cunningham, E. C., Deason, A. J., Rockosi, C. M., et al. 2019, ApJ, 876, 124
Deason, A. J., Belokurov, V., & Evans, N. W. 2011, MNRAS, 416, 2903
Deason, A. J., Belokurov, V., Evans, N. W., & An, J. 2012, MNRAS, 424, L44
Deason, A. J., Belokurov, V., Evans, N. W., & Johnston, K. V. 2013a, ApJ, 763, 113
Deason, A. J., Belokurov, V., Koposov, S. E., & Lancaster, L. 2018, ApJL, 862, L1
Deason, A. J., Belokurov, V., & Weisz, D. R. 2015, MNRAS, 448, L77
Deason, A. J., Van der Marel, R. P., Guhathakurta, P., Sohn, S. T., & Brown, T. M. 2013b, ApJ, 766, 24
Dehnen, W., McLaughlin, D. E., & Sachania, J. 2006, MNRAS, 369, 1688
Eadie, G., Keller, B., & Harris, W. E. 2018, ApJ, 865, 72
Eadie, G. M., Springford, A., & Harris, W. E. 2017, ApJ, 835, 167
Escala, I., Wetzel, A., Kirby, E. N., et al. 2018, MNRAS, 474, 2194
Foreman-Mackey, D., Hogg, D. W., Lang, D., & Goodman, J. 2013, PASP, 125, 306
Gaia Collaboration, Brown, A. G. A., Vallenari, A., et al. 2018a, A&A, 616, A1
Gaia Collaboration, Helmi, A., van Leeuwen, F., et al. 2018b, A&A, 616, A12
Gaia Collaboration, Prusti, T., de Bruijne, J. H. J., et al. 2016, A&A, 595, A1
Garrison-Kimmel, S., Hopkins, P. F., Wetzel, A., et al. 2019, MNRAS, 487, 1380
Gillessen, S., Eisenhauer, F., Trippe, S., et al. 2009, ApJ, 692, 1075
Gnedin, O. Y., Brown, W. R., Geller, M. J., & Kenyon, S. J. 2010, ApJL, 720, L108
Hattori, K., Valluri, M., Loebman, S. R., & Bell, E. F. 2017, ApJ, 841, 91
Helmi, A., Babusiaux, C., Koppelman, H. H., et al. 2018, Natur, 563, 85
Hopkins, P. F. 2015, MNRAS, 450, 53
Hopkins, P. F., Wetzel, A., Kereš, D., et al. 2018, MNRAS, 480, 800
Jeans, J. H. 1915, MNRAS, 76, 70
Kafle, P. R., Sharma, S., Lewis, G. F., & Bland-Hawthorn, J. 2012, ApJ, 761, 98
Kafle, P. R., Sharma, S., Robotham, A. S. G., Elahi, P. J., & Driver, S. P. 2018, MNRAS, 475, 4434
King, C. I., Brown, W. R., Geller, M. J., & Kenyon, S. J. 2015, ApJ, 813, 89
Lancaster, L., Koposov, S. E., Belokurov, V., Evans, N. W., & Deason, A. J. 2019, MNRAS, 486, 378
Laporte, C. F. P., Johnston, K. V., Gómez, F. A., Garavito-Camargo, N., & Besla, G. 2018, MNRAS, 481, 286
Loebman, S. R., Valluri, M., Hattori, K., et al. 2018, ApJ, 853, 196
Mahmud, N., & Anderson, J. 2008, PASP, 120, 907
Price-Whelan, A. M., Johnston, K. V., Sheffield, A. A., Laporte, C. F. P., & Sesar, B. 2015, MNRAS, 452, 676
Rashkov, V., Pillepich, A., Deason, A. J., et al. 2013, ApJL, 773, L32
Robin, A. C., Reylé, C., Derrière, S., & Picaud, S. 2003, A&A, 409, 523
Sales, L. V., Navarro, J. F., Abadi, M. G., & Steinmetz, M. 2007, MNRAS, 379, 1464
Sanderson, R. E., Garrison-Kimmel, S., Wetzel, A., et al. 2018a, ApJ, 869, 12
Sanderson, R. E., Wetzel, A., Loebman, S., et al. 2018b, arXiv:1806.10564
Schönrich, R., Binney, J., & Dehnen, W. 2010, MNRAS, 403, 1829
Sesar, B., Jurić, M., & Ivezić, Ž. 2011, ApJ, 731, 4
Sirko, E., Goodman, J., Knapp, G. R., et al. 2004, AJ, 127, 914
Smith, M. C., Evans, N. W., Belokurov, V., et al. 2009, MNRAS, 399, 1223
Sohn, S. T., Anderson, J., & van der Marel, R. P. 2012, ApJ, 753, 7
Sohn, S. T., Besla, G., van der Marel, R. P., et al. 2013, ApJ, 768, 139
Sohn, S. T., Patel, E., Besla, G., et al. 2017, ApJ, 849, 93
Sohn, S. T., van der Marel, R. P., Carlin, J. L., et al. 2015, ApJ, 803, 56
Sohn, S. T., van der Marel, R. P., Kallivayalil, N., et al. 2016, ApJ, 833, 235
Sohn, S. T., Watkins, L. L., Fardal, M. A., et al. 2018, ApJ, 862, 52
VandenBerg, D. A., Bergbusch, P. A., & Dowler, P. D. 2006, ApJS, 162, 375
Wang, W., Han, J., Cole, S., et al. 2018, MNRAS, 476, 5669
Watkins, L. L., Evans, N. W., Belokurov, V., et al. 2009, MNRAS, 398, 1757
Watkins, L. L., van der Marel, R. P., Sohn, S. T., & Evans, N. W. 2019, ApJ, 873, 118
Wetzel, A. R., Hopkins, P. F., Kim, J.-h., et al. 2016, ApJL, 827, L23